Chapter 5

One-Pot *N*-Alkylation Reaction over Reusable Ni(II) Decorated MOP-Am2 *via* Borrowing Hydrogen Strategy

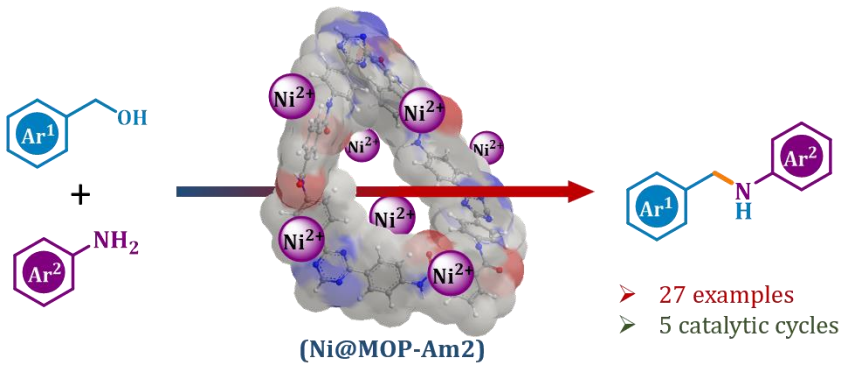

5.1 Introduction

The C–N bond formation reaction is one of the most ubiquitous reactions in organic synthesis that provides access to all kinds of amines [1-3]. Being an integral part of most of the drugs and bioactive molecules, amines are indispensable bulk chemicals for dyes, agrochemicals, lubricants, surfactants, etc. and have been used as precursors in many daily products [4]. Based on the widespread potency of C–N bonds, the development of a greener and more efficient methodology has become one of the sought research goals. Known classical methods of C–N bond formation is majorly occupied by three name reactions: Buchwald-Hartwig amination, Chan-Lam coupling and Ullmann reactions [5-7]. Most of the reported traditional methods suffer from uncontrollable side products, selectivity and inevitably generate stoichiometric waste. Notably, the exploration of direct *N*-alkylation from alcohols received tremendous attention as a renewable feedstock obtained from lignocellulose, nontoxic, easily available and easy to handle [8,9]. General strategy is the dehydrogenation of alcohols to comparatively more reactive carbonyl compounds and condensation with amines to corresponding imine intermediates followed by reduction of C=N moiety. Further improvement involves catalytic protocol where a transition metal catalyst captures the dehydrogenated H_2 during the oxidation of alcohols and transfers it to the hydrogenation step of imine intermediates. This protocol is known as the "hydrogen auto-transfer" or "borrowing hydrogen", first coined the term by Williams in 2004 [10,11].

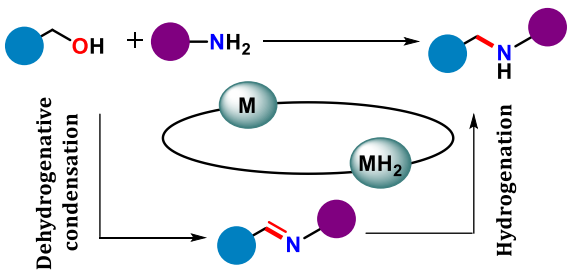

Figure 5.1 Schematic representation of three steps amine formation *via* borrowing hydrogen strategy

Borrowing hydrogenation, since its discovery, has become an important alternative tandem process for any kind of *N*-alkylation. Substitution by alcohols instead of more reactive carbonyl compounds through borrowing hydrogen strategy is now one of the most attentive green chemistry approaches. The basic idea of borrowing

hydrogen strategy is that the alcohol will first undergo dehydrogenative oxidation to its corresponding carbonyl compound. It undergoes imine condensation with the existing amine and then finally the hydrogenation of the imine to yield the desired *N*-alkylated amine (Figure 5.1). The high abundance and inexpensive alcohols offer improved step efficiency over the conventional stoichiometric activation. Indeed, this avoids the sulfonate esters or the mutagenic alkyl halides as alkylating agents. Eventually, the elimination of H_2O as the only waste in this strategy makes the protocol environmentally the most benign method for *N*-alkylation.

Nevertheless, the metal catalysed borrowing approach is a sustainable and elegant technology for C–N bond forming reactions. Reports unveiled the use of a diverse range of catalytic systems composed of precious metal like Ru, Ir, Os, Pd and so forth that serves as hydrogen carrier in borrowing hydrogen strategy [12-16]. But aiming for the development of earth abundant, less toxic, cheap and sustainable metal catalysts would be highly desirable. Indeed, significant progress has been made in *N*-alkylation reactions with first-row transition metals like Fe, Co, Cu, and Mn [17,18]. In fact, Beller and Milstein's, work on *N*-alkylation reaction with Mn-pincer complexes is worth mentioning [19,20]. Besides high natural abundance and low toxicity, nickel would serve as a potential support for *N*-alkylation reaction [21]. Nickel acts as a sustainable alternative to palladium in the Buchwald–Hartwig coupling reaction because of its modular redox properties. [22,23] However such examples are elusive and sparse to date. Recently, Banerjee and coworkers reported the first homogeneous nickel species for *N*-alkylation reaction [24]. But major drawbacks lie in its stability and recyclability. Following few heterogeneous Ni species has been reported with limited substrate scope and very harsh synthetic procedure. Barta and coworkers reported the mono alkylation of amine catalysed by an unprecedented *in-situ* formation of Ni nanoparticles in the presence of a stoichiometric base [25]. Further Yus and coworkers illustrated the use of Ni nanoparticles as support in *N*-alkylation where isopropanol had been used as an external source of hydrogen [26]. Despite the indisputable advances, it still suffered from hitches like the use of expensive ligands, base stoichiometry, high catalyst dosages, harsh reaction conditions and catalyst recovery. Recent breakthrough by Namitharan and coworkers demonstrated a metal free protocol where pyridine was

used as a mediator for *N*-alkylation reaction. But again, it suffers from chemical hazards and high temperature. Therefore, the finding of environmentally benign and affordable protocol for *N*-alkylation reaction becomes an important concern.

A. Ru-catalyzed *N*-alkylation of amines [12].

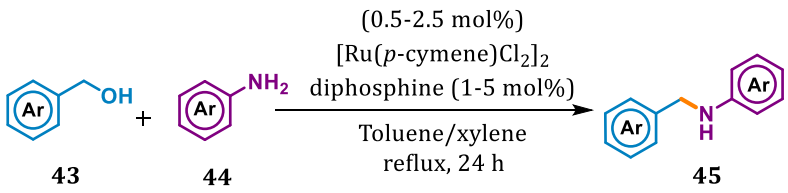

B. Ir-catalyzed *N*-alkylation of amines [12].

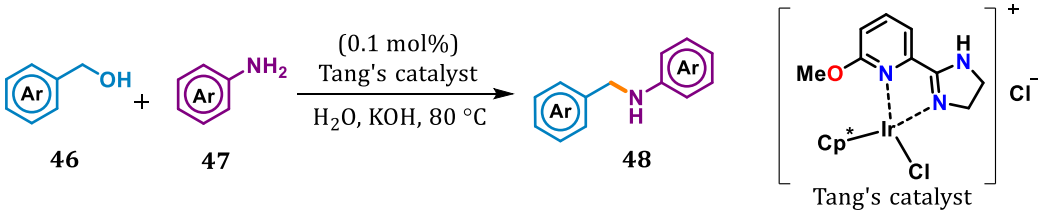

C. Mn-pincer complex catalysed *N*-alkylation of amines [19].

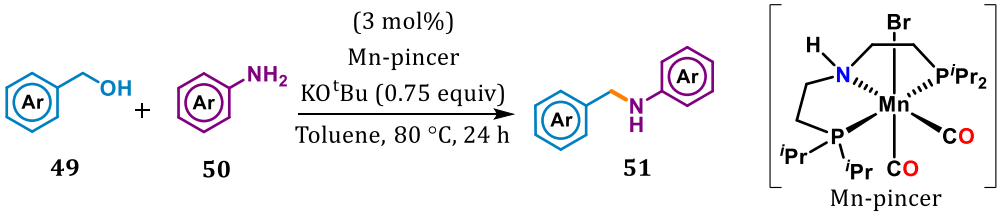

D. Homogeneous Ni-catalysed *N*-alkylation of amines [24].

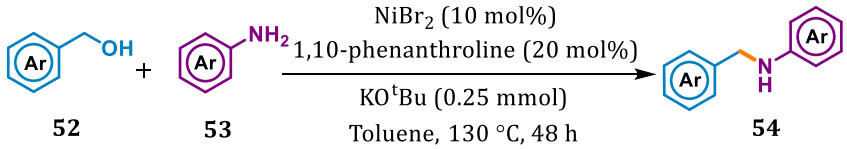

E. Pyridine-catalysed *N*-alkylation of amines.

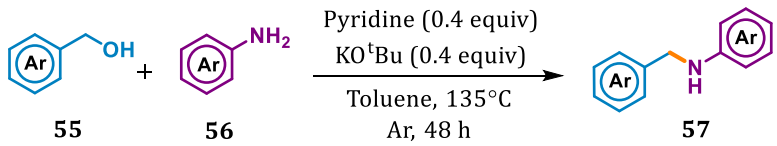

While using numerous catalytic systems for *N*-alkylation reactions, porous organic polymers (POPs) as heterogeneous support, despite their rising applications, for such reactions are still unknown. Literature evinced the accomplishment of organic reactions driven by POPs as organocatalysts or as a support matrix for metal incorporation that are promising hosts in heterogeneous catalysis. Among them

phosphine free Suzuki-Miyaura cross-coupling, Heck reaction, Heck-Matsuda reaction, Sonogashira reaction, nitroarene reduction, Chan-Lam coupling, asymmetric synthesis, etc. are worth mentioning [27-30]. Recently Maji and coworkers implemented POP with dual metalation *i.e.* Ir and Ni in heterogeneous catalytic C–N coupling reaction under visible light [31].

In Chapter 3 & 4, we explored MOP-Am2 as an excellent catalytic bed for the anaerobic oxidation of alcohols. During the reactions, the elimination of H_2 is obvious as a side product that was found difficult to store or utilize in some other reactions. The presence of high nitrogen content, porous nature and extended π-conjugation makes MOP-Am2 a competent host for metal impregnation. Based on the catalytic potency of inexpensive Ni ion and the targeted objectives of the work, herein we have presented the MOP-Am2 decorated with nickel precursor (Ni@MOP-Am2) to reuse the exerted H_2 in *N*-alkylation reaction (Scheme 5.1).

This work

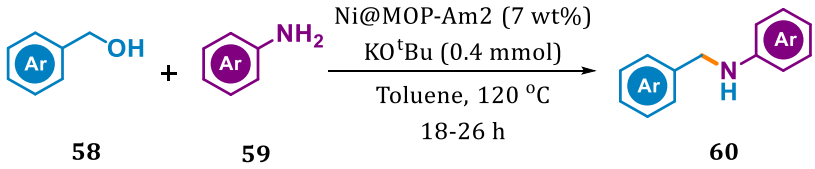

Scheme 5.1 *N*-alkylation of amine over Ni@MOP-am2 *via* borrowing hydrogen strategy

In accordance with our expectations, the optimal Ni@MOP-Am2 showed excellent catalytic performance and could be effectively recycled and reused.

5.2 Results and Discussion

5.2.1 Synthesis of Ni(II) decorated MOP-Am2

To construct the Ni(II) decorated MOP-Am2, a similar strategy has been reproducibly employed that was mentioned in Chapter 4 to obtain the precursor organocatalyst. The high nitrogen content, porous nature and extended π-conjugation made MOP-Am2 a competent host for nickel impregnation. To attain the targeted objectives of the work, MOP-Am2 was thus decorated with Ni(II) salt by treating it with $NiCl_2{\cdot}6H_2O$ in dichloromethane for 24 h (Scheme 5.2). The resulting reaction mixture was filtered, washed thoroughly with distilled water to remove the excess Ni(II) salts

and dried in an oven at 100 °C for 24 h. The desired insoluble dark yellow powder, Ni@MOP-Am2 was characterized accordingly.

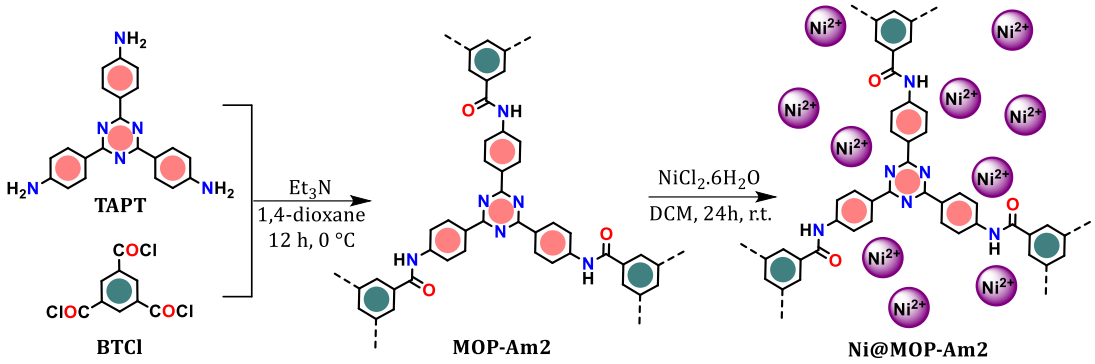

Scheme 5.2 Schematic representation of the synthesis of Ni(II) decorated porous organic polymer, Ni@MOP-Am2

Overlay of the FT-IR analysis of both MOP-Am2 and Ni@MOP-Am2, the stretching frequency at 1665 and 3363 cm^{-1} responsible for carboxamide (–HN–C=O) retained in both the materials (Figure 5.2a). In fact, it was evident that no significant changes occurred in the structural skeleton during metal incorporation. The overlay of the PXRD pattern (Figure 5.2b) also showed intact structural integrity with similar 2θ values at 6.85°, 9.13°, 24.68° and 43.41°. However, the broad signal for MOP-Am2 appeared at 2θ=15.74° has been observed with a small shifting to 16.09° in the case of Ni(II) incorporated material. Unfortunately, no significant peaks responsible for Ni(II) was observed which might suggest a limited loading of metal salt buried inside the pores of MOP-Am2 and dispersed in fine particles.

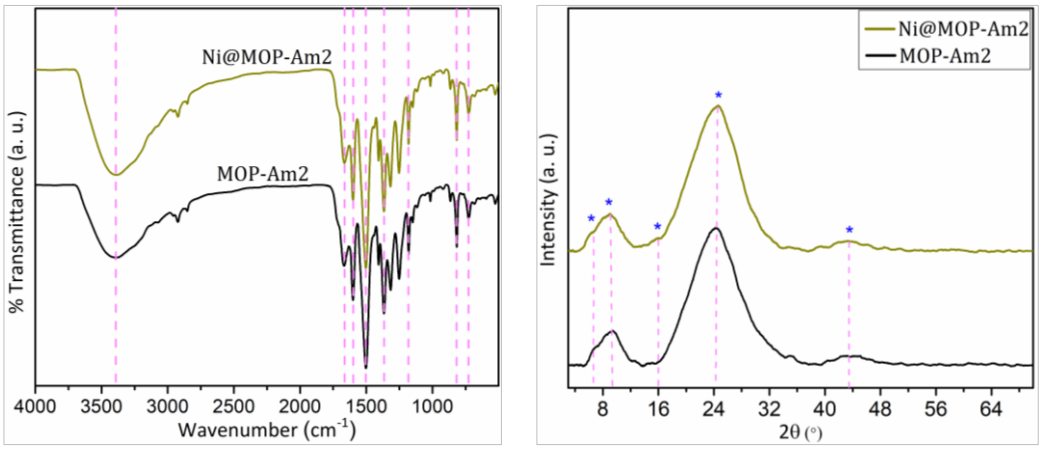

(a) (b)

Figure 5.2 Overlay FT-IR spectra (a) and PXRD pattern (b) of MOP-Am2 and Ni@MOP-Am2

The quantitative incorporation of Ni(II) was confirmed with the atomic adsorption spectroscopy (AAS) and was calculated to be 1.60%. Hence it is quite obvious to merge the characteristic peaks of Ni(II) in PXRD pattern under the broad signals of bare MOP-Am2.

Revisiting the surface behavior, BET analysis on bare MOP-Am2 demonstrated a type IV N_2 sorption isotherm having a calculated surface area of 90 m^2g^{-1} along with narrow pore width of 1.5 nm (Figure 5.3a,b). Upon impregnating nickel salts, the calculated surface area of Ni@MOP-Am2 was decreased to 78 m^2g^{-1}. This was obvious as the nickel salt started occupying the pores. At the same time the increase in pore width to 2.2 nm (Figure 5.3b) is attributed to the expansion of pore size due to the localization of Ni(II) salt into the pores. Hence the Ni(II) embedded MOP-Am2 is no longer microporous, but instead mesoporous in nature.

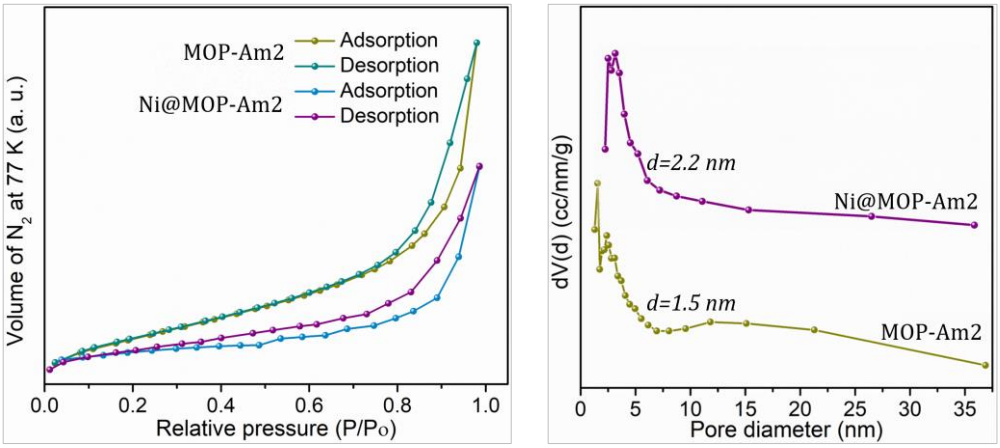

(a) (b)

Figure 5.3 N_2 sorption isotherm (a) and pore size distribution (PSD) plot (b) of MOP-Am2 and Ni@MOP-Am2

The surface morphological appearance for both the MOP-Am2 (Chapter 4, Figure 4.2a) and Ni@MOP-Am2 was compared using FESEM analysis. Figure 5.4a revealed that upon the incorporation of the metal salt, the globular texture of Ni@MOP-Am2 remained unchanged. This outcome supports the good agreement of the similar PXRD pattern of MOP-Am2 before and after the incorporation of metal salt. Besides the TEM analysis (Figure 5.4b) determined the expansion of polymeric hollow-spherical morphology compared to Figure 4.2b mentioned in Chapter 4. As we have already discussed the role of Oswald ripening on the formation of hollow-sphere, the metal incorporation might help in nucleating the polymeric material on the

periphery by non-covalent interaction of the metal ions over MOP-Am2. Perhaps the presence of nickel in Ni@MOP-Am2 was further observed with HR-TEM analysis that clearly interpreted the presence of lattice fringe responsible for nickel particles (Figure 5.4b).

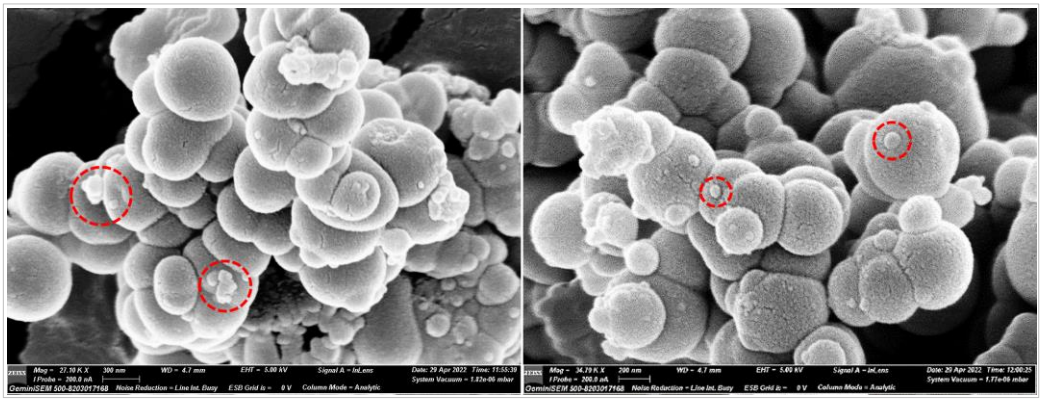

(a)

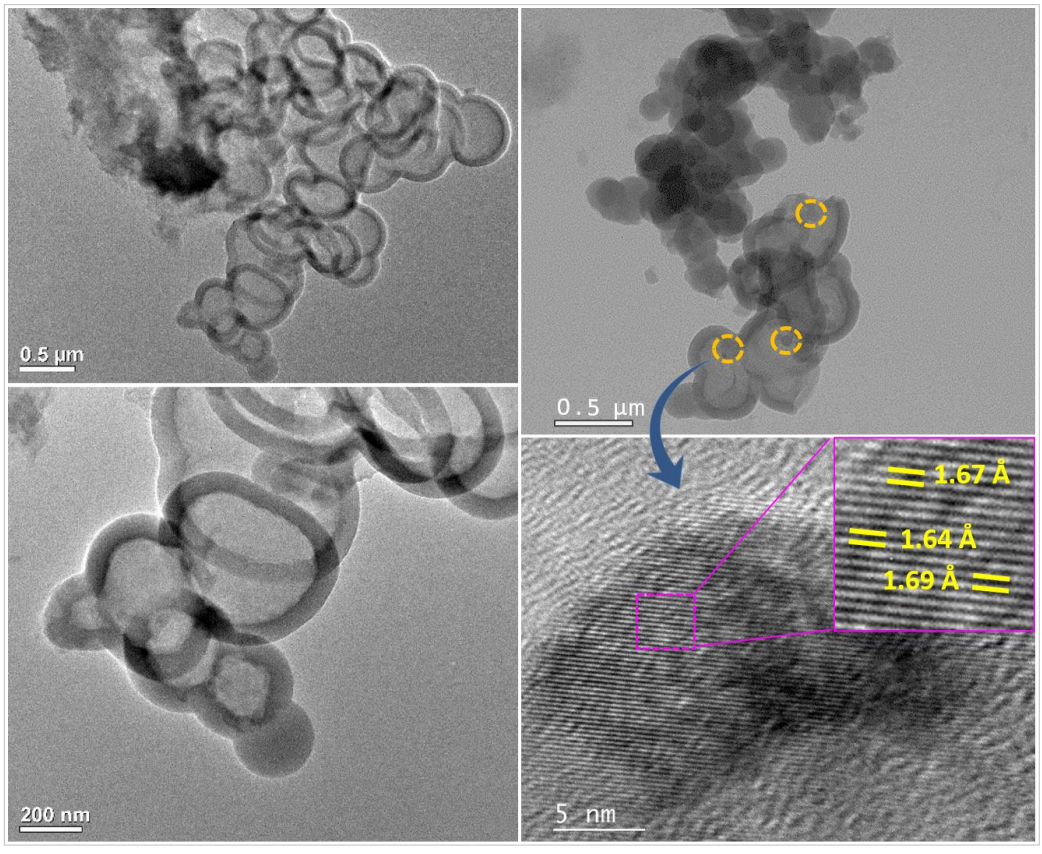

(b)

Figure 5.4 (a) FESEM analysis of Ni@MOP-Am2 suggested the intact globular rough surface with metal particle (red circle) on it. (b) TEM analysis of Ni@MOP-Am2 suggested expanded polymeric hollow-spherical morphology of the material. The presence of metal particles (yellow circle) was also prominent. HR-TEM analysis interpreted the presence of lattice fringe responsible for nickel particles

Moreover, the distribution of nickel along with other atoms was further analysed by recording the SEM-EDX elemental mapping of Ni@MOP-Am2. Figure 5.5 represented the uniform distribution of the atoms present. From the spectrum, the quantitative amount of nickel loaded on MOP-Am2 was calculated to be 1.66% by weight which further validated the result obtained from AAS analysis.

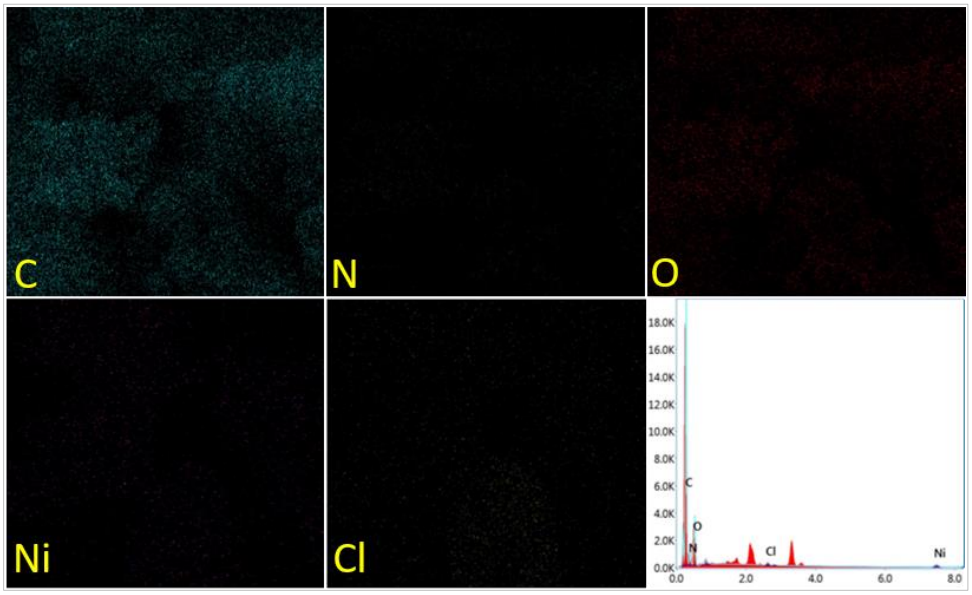

Figure 5.5 SEM-EDX elemental mapping and spectra of Ni@MOP-Am2

The chemical composition and the oxidation state of the metal ions at the surface of the catalyst, Ni@MOP-Am2 were investigated by X-ray photoelectron spectroscopy (XPS). The survey spectrum clearly depicted the existence of C, N, O, Ni and Cl atom in Ni@MOP-Am2 (Figure 5.6). The deconvoluted fitting high resolution XPS spectrum of C 1s showed four distinct peaks at 284.6 eV, 286.2 eV, 288.1 eV and 290.4 eV responsible for C=C (aromatic), C=N (triazine), CONH (amide) and C=C* (carbon under positive electron environment) respectively [32,33]. Similarly, the deconvolution fitting of N 1s XPS spectrum initially displayed two distinct peaks at 398.5 eV and 400.1 eV which were ascribed for C=N (triazine) and N–H (amide) respectively [34-36]. The available lone pair on triazine nitrogen has easy accessibility to co-ordinate with the metal ion making the triazine nitrogen $C=N^{+}$. Hence an additional peak at 401.7 eV was observed which might represent the C=N→Ni interaction. The deconvoluted fit of the XPS spectrum of O 1s, on the other hand, showed a distinct region of binding energy at 531.6 eV and 533.3 eV responsible for C=O and O–H respectively [37]. This clearly indicated that the lone

pair present on nitrogen in the amide group was under delocalization with C=O. Hence, the interaction of the metal ion over amide functionality from either the oxygen or nitrogen site has a low probability.

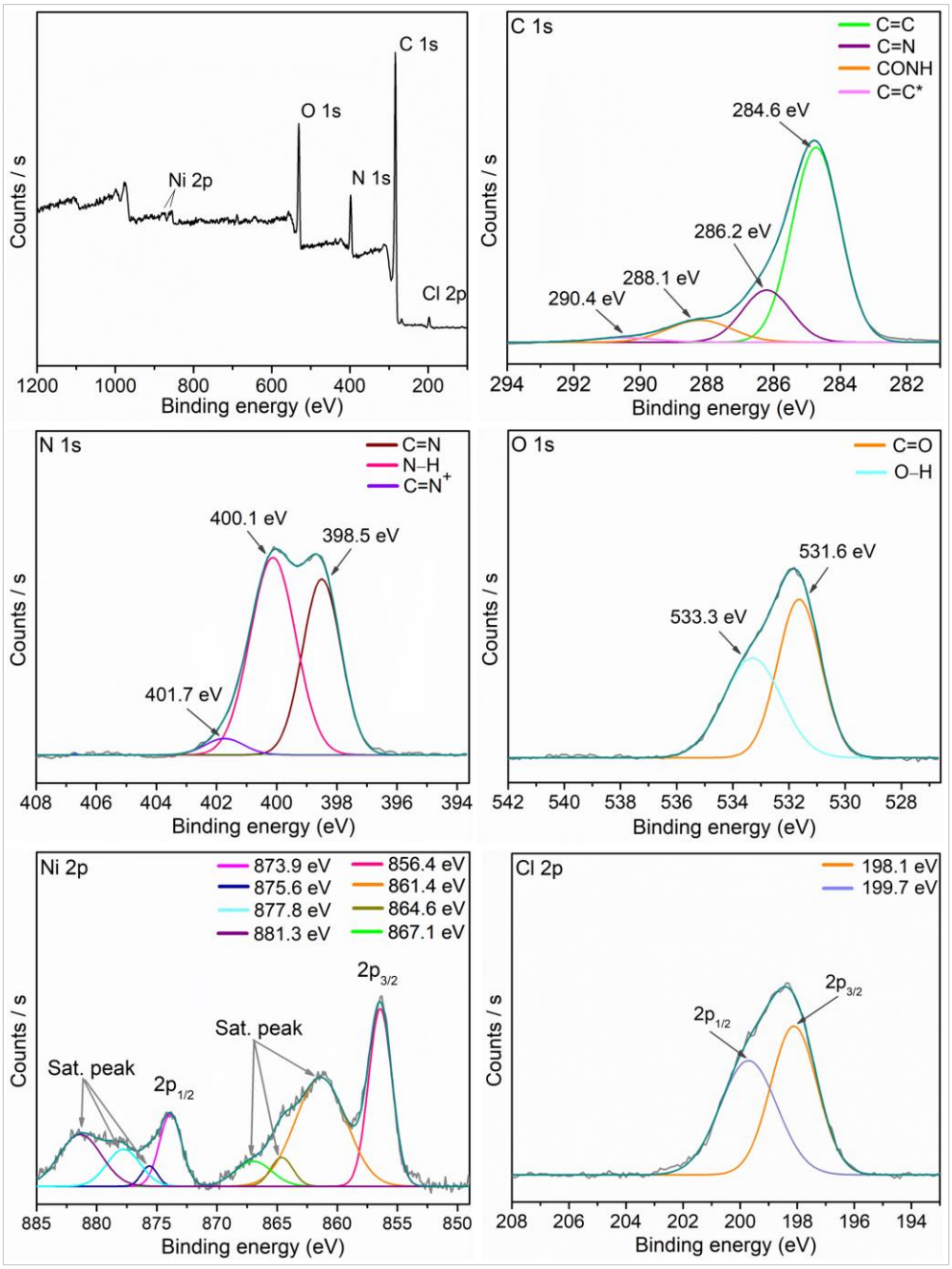

Figure 5.6 XPS spectra of overall survey, C 1s, N 1s, O 1s, Ni 2p and Cl 2p of Ni@MOP-Am2

Meanwhile, the deconvoluted Ni 2p spectrum, demonstrated two binding energies centered at around 856.4 eV and 873.9 eV ascribed from Ni $2p_{3/2}$ and Ni $2p_{1/2}$ respectively along with six satellite peaks at around 861.4 eV, 864.6 eV, 867.1 eV,

875.6 eV, 877.8 eV and 881.3 eV. This clearly confirmed the existence of Ni in the +2 oxidation state in Ni@MOP-Am2. Again, the two deconvoluted signals in the fine Cl 2p spectrum at 198.1 eV and 199.7 eV are ascribed for Ni–Cl which maintain the overall oxidation state of the metal ion

Quantum mechanical calculation with the density functional theory (DFT) was performed to get further insight into the active binding sites and the interactions of MOP-Am2 with Ni(II). With limited competence it was difficult to carry out a computational study on the catalytic behavior of the Ni(II) embedded polymeric MOP-Am2. Since the MOP-Am2-m is essentially an active catalyst for the reactions studied, we reflected the same in place of the MOP-Am2 structure for calculation. The structural optimization and various active binding sites of MOP-Am2-m for the interaction with $NiCl_2$ were carried out using the B3LYP/6-31G(d) level of theory.

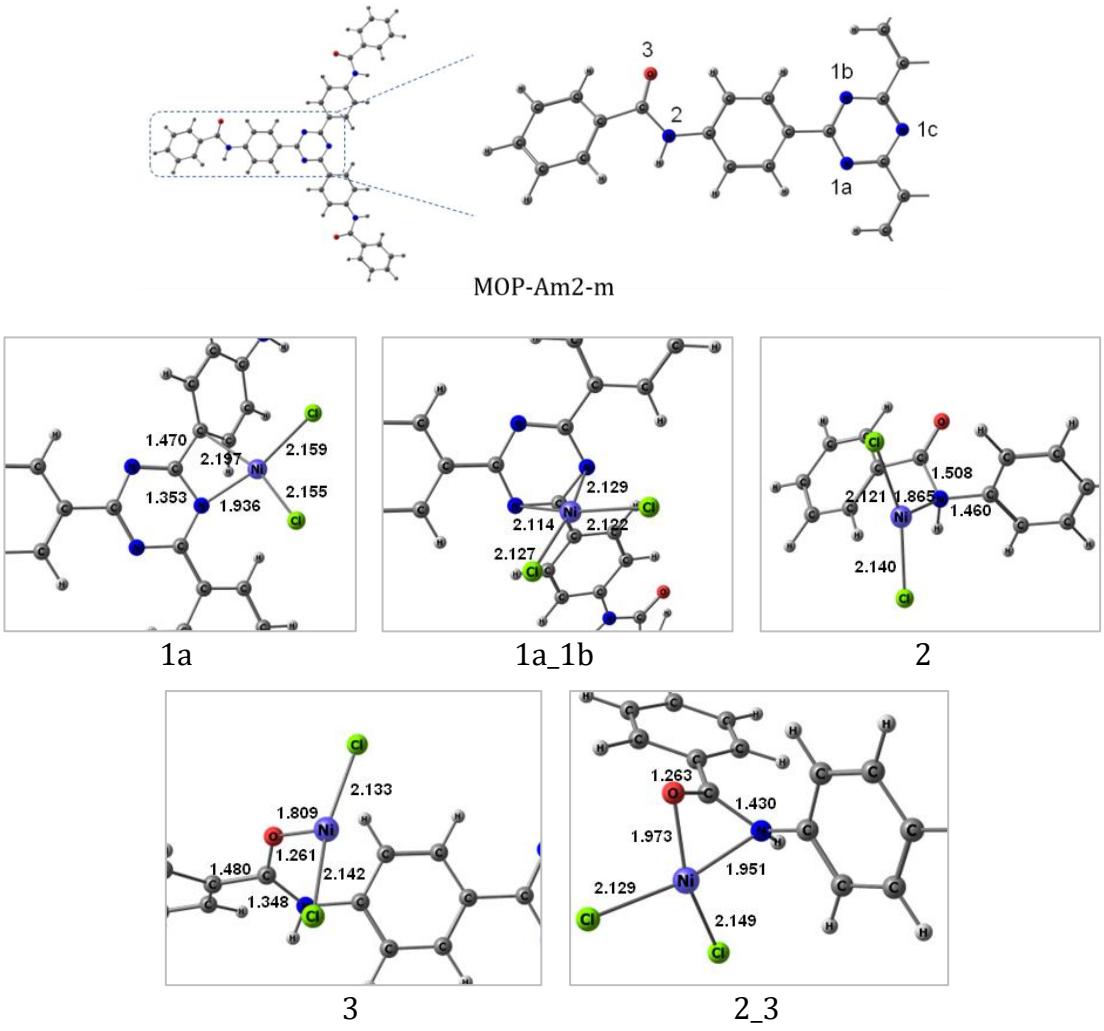

Figure 5.7 Optimized geometry of MOP-Am2-m unit along with its different binding sites for the interaction with Ni(II) as $NiCl_2$ [Active sites are labeled as 1-3]

Considering the structure of MOP-Am2-m unit, there are three possible active sites, nitrogen atom of triazine moiety (1) and both the nitrogen (2) and oxygen (3) present in amide linkage (Figure 5.7). Since, three N atoms of triazine are equivalent in nature; they are labeled as 1a, 1b and 1c. Hence, five different configurations are obtained based on the interactions between three active sites and $NiCl_2$. The adsorption energy (E_{ads}) for the interaction of $NiCl_2$ with 1a active site is –49.65 kcal/mol. It is important to note that $NiCl_2$ interacts with the N atom of triazine as well as the partial double bond of the *ipso*- and *ortho*-C atom of the closest benzene ring in the 1a configuration. The distance of the Ni–N bond and the Ni–C bond are 1.936 Å and 2.197 Å, respectively. This outcome also validated the XPS data of C 1s at 290.4 eV. When $NiCl_2$ interacts with two of the N atoms of the triazine moiety, it leads to the configuration of 1a_1b. The adsorption energy for this configuration is –29.65 kcal/mol. The two Ni–N bond lengths are 2.114 Å and 2.129 Å. On interacting with all the three N atoms of triazine, the optimized structure leads to the same configuration as that of 1a_1b. Configuration 2 occurs when Ni(II) attacks the N atom of amide group resulting in the E_{ads}= –36.93 kcal/mol. The two Ni–Cl bonds are about 2.121 Å and 2.140 Å while the Ni–N bond is 1.865 Å. When Ni(II) attacks the O atom of the same amide group (Configuration 3), it results in the E_{ads}= –42.00 kcal/mol. Elongation of C–O bond occurs from 1.224 Å to 1.261 Å. Strong Ni–O bond is formed which is evident from the bond length (1.809 Å). At last, another configuration arises (Configuration 2_3) when both N and O atoms of the amide group are interacting with Ni(II) having E_{ads}= –40.32 kcal/mol. Therefore, the most dominant configuration is 1a where Ni(II) interacts with the N atom of triazine as well as an *ortho*-C atom of nearby benzene.

For any given catalyst, its stability is an important aspect to allow for cost-efficient applications. The high thermal stability with no weight loss and insolubility in most of the common organic and inorganic solvents renders Ni@MOP-Am2 a potential candidate for heterogeneous catalysis.

5.2.2 Catalytic study of Ni@MOP-Am2

The crucial task in direct *N*-alkylation using alcohols was to attain alcohol dehydrogenation and the ability of the *in-situ* formed H_2 for imine hydrogenation.

Our previous studies in Chapter 2 & 3 indeed succeeded to establish the evolution of H_2 from alcohols over metal free MOP-Am2. Unfortunately, we failed to hydrogenate the imine for direct *N*-alkylation with bare MOP-Am2 due to the lack of proper source to capture the *in-situ* formed H_2. In the exploration of the ability of Ni(II)@MOP-Am2, 4-methylbenzyl alcohol (**61**) with aniline (**62**) to form *N*-(4-methylbenzyl)aniline (**63**) was chosen as a benchmark reaction. To achieve the optimal reaction conditions, based on the reported procedure, the reaction was initially started with 0.5 mmol of **61** and 0.5 mmol of **62** taken in a schlenk tube with 1 mmol of potassium *tert*-butoxide (KO^tBu), 15% (w/w) of Ni@MOP-Am2, 1 mL of toluene as solvent and the whole system is degassed and heated at 140 °C for 24 h. Despite the suitable conversions towards **63** confirmed with ^1H NMR spectroscopy, the selectivity was conceded. Nearly 50% of the imine intermediate (**64**) during the reaction was left over. In a recent study by Boronat and coworkers drew an interesting summary *via* NMR spectroscopy analysis that the H_2 that is used for the hydrogenation of imine intermediate comes from the methylene hydrogen of the alcohol [38]. Hence it is mandatory to use at least two equivalents of **61** against **62**. With this modified protocol, we have examined the reaction with two equivalents of **61**. Interestingly selectivity towards **63** changed predominantly. Upon further increasing the concentration of **61** to 2.2 equivalent, only a trace amount of **64** left over which remained unchanged even after enhancing the stoichiometry of **61**.

With the stoichiometry optimization, the responsible elements like oxidation source, sacrificial agents and catalyst necessities were resolved accordingly and presented in Table 5.1. To attain these goals, we initiated our investigations with 15% of Ni@MOP-Am2, 1 mmol KO^tBu, 1.1 mmol of **61**, 0.5 mmol of **62** and 1 mL of toluene under the degassed condition at 140 °C resulted in 95% yield (Table 5.1, entry 1) confirmed with ^1H NMR analysis. Besides the same reaction condition with xylene and mesitylene as solvents gave poorer results, 38% and 40% respectively (Table 5.1, entry 2-3). On the other hand, acetonitrile, DMF and 1,4-dioxane did not promote the reaction (Table 5.1, entry 4-6) while DMSO responded with trace conversion (Table 5.1, entry 7). Selecting toluene for further study, the effect of bases and their stoichiometry were evaluated (Table 1, entry 8-16). The reaction did not proceed in absence of the base (Table 5.1, entry 8) which signified that base was an essential

and sacrificial element for the conversion. Besides good conversion with NaOH and KOH, high imine selectivity, **64** remained unreacted in the reaction mixture. In addition, the decrease in KO^{t}Bu to 0.3 mmol dropped the yield to 78%. In fact, the best result was found at 0.4 mmol of KO^{t}Bu (Table 5.1, entry 16).

To affirm the reaction was indeed driven by Ni@MOP-Am2, we accompanied the catalyst loading optimization (Table 5.1, entry 17-21). Interestingly lowering the catalyst amount to 5% with respect to **61**, almost 88% of it was converted but the selectivity of **63** was only 71% while the rest of the conversion persisted as **64**. This clearly suggested that the oxidation of **61** to its corresponding carbonyl compound can be carried out even in bare MOP-Am2, while the presence of Ni(II) plays an imperative role in the hydrogenation of **64**. The two individual steps involved in the reaction were clearly identified while optimizing the temperature (Table 5.1, entry 22-28). Indeed, at temperature 90-100 °C only **64** was obtained predominantly. With increasing the temperature to 110-120 °C, hydrogenation dominates the reaction to give **63**.

Table 5.1 Reaction optimization for *N*-alkylation with 4-methylbenzyl alcohol.[a]

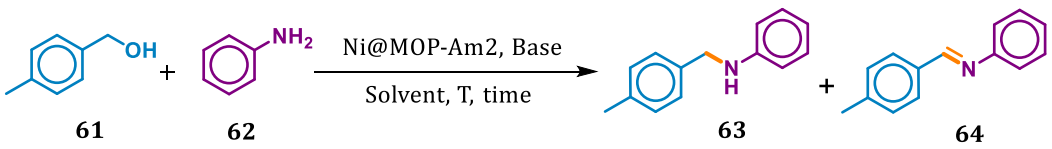

61 **62** **63** **64**

Entry	Cat. % (w/w)	Base (mmol)	Solvent	Temperature (°C)	**63**; % Yield[b] (Selectivity)
1	15	KO^{t}Bu (1)	Toluene	140	95 (>99)
2	15	KO^{t}Bu (1)	Xylene	140	38 (98)
3	15	KO^{t}Bu (1)	Mesitylene	140	40 (99)
4	15	KO^{t}Bu (1)	MeCN	140	NR
5	15	KO^{t}Bu (1)	DMF	140	NR
6	15	KO^{t}Bu (1)	1,4-dioxane	140	NR
7	15	KO^{t}Bu (1)	DMSO	140	Trace
8	15	-	Toluene	140	NR
9	15	Cs_2CO_3 (1)	Toluene	140	NR
10	15	NaOH (1)	Toluene	140	41 (55)

11	15	KOH (1)	Toluene	140	49 (60)
12	15	DBU (1)	Toluene	140	NR
13	15	DMAP (1)	Toluene	140	NR
14	15	KO^{t}Bu (0.5)	Toluene	140	95 (99)
15	15	KO^{t}Bu (0.4)	Toluene	140	94 (99)
16	15	KO^{t}Bu (0.3)	Toluene	140	78 (99)
17	-	KO^{t}Bu (0.4)	Toluene	140	NR
18	12	KO^{t}Bu (0.4)	Toluene	140	94 (99)
19	10	KO^{t}Bu (0.4)	Toluene	140	94 (99)
20	7	KO^{t}Bu (0.4)	Toluene	140	94 (99)
21	5	KO^{t}Bu (0.4)	Toluene	140	88 (71)
22	7	KO^{t}Bu (0.4)	Toluene	90	*
23	7	KO^{t}Bu (0.4)	Toluene	100	*
26	7	KO^{t}Bu (0.4)	Toluene	110	77 (82)
27	7	KO^{t}Bu (0.4)	Toluene	120	94 (99)
28	7	KO^{t}Bu (0.4)	Toluene	130	94 (99)

[a]Reaction condition: **61** (1.1 mmol), **62** (0.5 mmol), 7% (w/w) Ni@MOP-Am2 w. r. t. **61**, KO^{t}Bu (0.4 mmol), Toluene (1-2 mL), T (120 °C), time (18 h). [b]Yield determined by ^{1}H NMR. NR= No reaction. *Only **64** formed.

Notably, in absence of either the base or the catalyst (Table 5.1, entry 8 & 17), the reaction was negative. This suggested that the combination of base and Ni@MOP-Am2 was an essential component of the reaction. This fascinating combination of base and the catalyst not only process the anaerobic oxidative imine condensation but the hydrogenation also where Ni(II) acts as carrier agent for H_2. Identifying the optimized reaction conditions, the supremacy and limitations of the protocol are checked with diverse alcohols and amines.

5.2.3 Substrate scope for *N*-alkylation with various amines

A wide range of substituted anilines/amine bearing both electron donating/ withdrawing substituents, halogenated and sterically hindered reactants have been tested for *N*-alkylation with **61** and their isolated yield (isolated yield) are listed in Table 5.2. No significant changes in the product formation have been observed for

electron donating substituents on aniline resulting in 95-97% yield when compared to unsubstituted aniline (**66a-e**). However, effect of the steric factor was observed in case of 2,4-dimethylaniline (**66f**, 91%).

Table 5.2 Substrate scope of amines for *N*-alkylation reaction and their corresponding crude yield (isolated yield).[a]

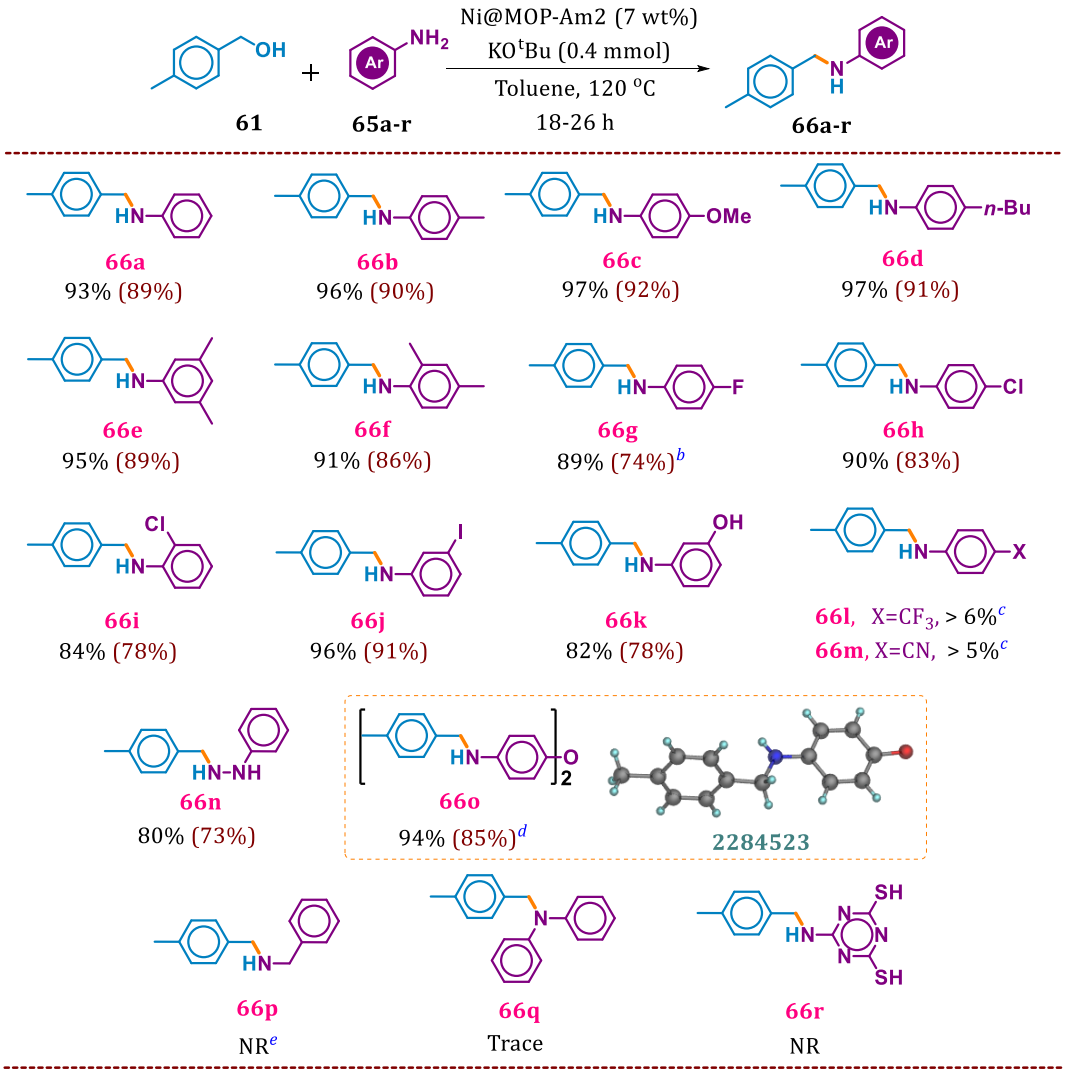

[a]Reaction condition: **61** (1.1 mmol), **65a-r** (0.5 mmol), 7% (w/w) Ni@MOP-Am2, KO^{t}Bu (0.4 mmol), Toluene (1-2 mL), Temperature (120 °C), Time (18-26 h). [b]Trace aldehyde remains intact because of the similar polarity. [c]Calculated from GCMS. [d]**65o** (0.25 mmol). [e]Imine formation. NR = No reaction.

Similar behaviour was also observed with halogen substituent on aniline (**66g-j**). Both *p*-fluoroaniline and *p*-chloroaniline demonstrated similar reactivity resulting conversion yield of 89-90%. Unfortunately, the isolated yield for **66g** was somewhat lower than the expected due to low polarity difference between the desired product

and the carbonyl intermediate. However, a gradual decrease in reactivity was observed in case of *o*-chloroaniline (**66i**, 84%) due to the steric factor, whereas significant increase in reactivity was observed in case of *m*-iodoaniline (**66j**, 96%). Further investigation with the electron withdrawing *m*-hydroxy substituent on aniline, the reactivity was found relatively low (**66k**, 82%). In fact, bearing *p*-trifluoromethyl- and *p*-cyano- substituent, the reaction proceeded with negligible conversion (**66l-m**). This implies higher the electron rich aniline, more prone to react with **61**.

We have also investigated the multifunctional anilines to find out the diversity of the protocol. Phenylhydrazine was also well tolerated with to furnish 80% product yield (**29n**). When diamine was used as substrate molecule, prominent conversion of *N,N'*-dialkylation was observed (**29o**, 94%). The limitation of the protocol was further investigated with aliphatic amine (Benzylamine) which did not proceed the reaction to give the desired *N*-benzylated product. Instead, the reaction stopped at detectable amount of imine intermediate. This is attributed to the tendency of aliphatic amine to coordinate with Ni(II) diminishing its activity [25]. Under identical condition, we observed a trace of desired product while using secondary amine (**29q**). Unfortunately, when multifunctional heterocyclic aniline was examined for *N*-alkylation, the reaction did not furnish the desired product (**29r**) under identical reaction conditions.

5.2.4 Substrate scope for *N*-alkylation with various alcohols

Further exploring the generality of the reaction, we also verified the scope of various primary, secondary and aliphatic alcohols and are listed in Table 5.3. Both substituted and unsubstituted alcohols were well tolerated for the catalytic *N*-alkylation reaction under the optimized reaction conditions. Electron donating substituents on benzyl alcohols yielded excellent productivity of 94-96% (**66b, 69a-b**). Notably the alcohols bearing the halogen at the aryl ring also tolerated well to good yield (**69c**). In fact, aliphatic alcohols also competed with the protocol (**32d**).

The fused alcohol such as 1-naphthyl methanol also tolerated well for *N*-alkylation (**69e**) despite having steric hindrance due to the fused aromatic ring at the *ortho*-

position. Surprisingly having steric factor, diphenyl methanol also furnished excellent catalytic activity with 96% yield (**69f**).

Table 5.3 Substrate scope of alcohols for *N*-alkylation reaction and their corresponding crude yield (isolated yield).[a]

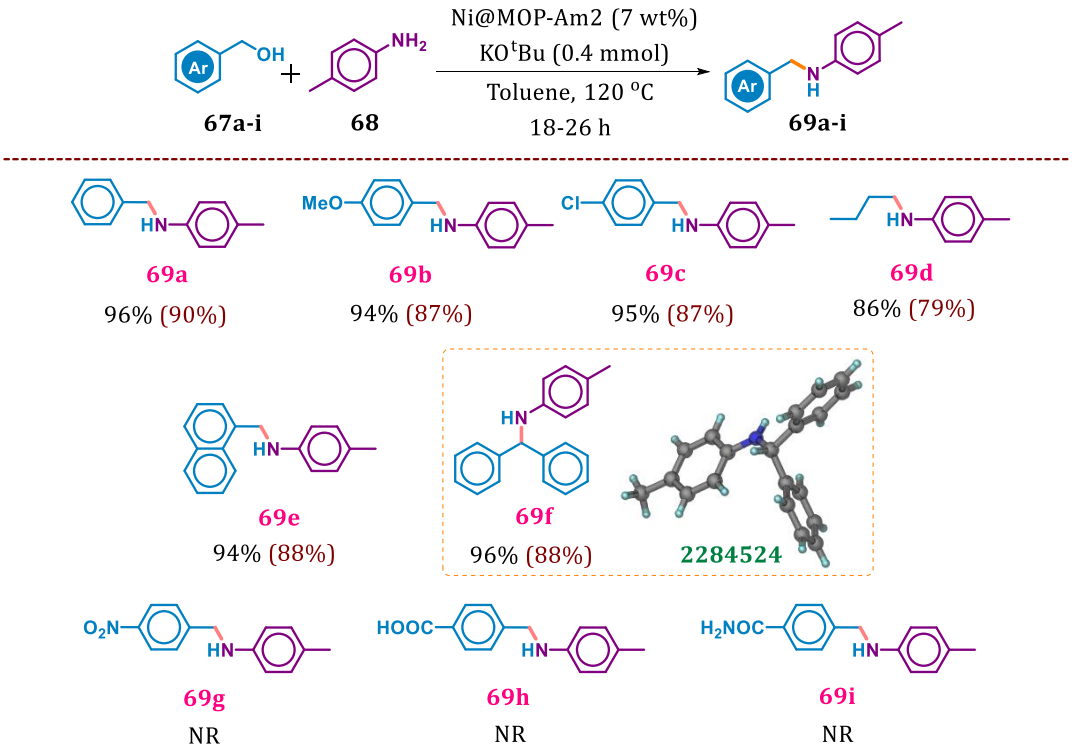

[a]Reaction condition: **67a-i** (1.1 mmol), **68** (0.5 mmol), 7 wt% Ni@MOP-Am2, KO^{t}Bu (0.4 mmol), Toluene (1 mL), Temperature (120 °C), Time (18-26 h). NR = No reaction.

However, attempt to electron withdrawing substituents such as $-NO_2$, –COOH, $-CONH_2$ on alcohols were unsuccessful (**69g-i**). It is noteworthy to allusion that the current catalytic route is highly selective for mono alkylation even after having excess carbonyl intermediate unreacted.

5.2.5 Mechanism study

Computational study has been performed to dig into the mechanism of the transformation reaction. The Gibbs' free energy values for all the intermediates and transition states involved in the reaction were obtained at 298 K and 1 atm. All structures are optimized with B3LYP/6-31G(d) level of theory. The optimized geometries of stable intermediates (IMs) as well as the transition state (TS) involved in the reaction are shown in Figure 5.8.

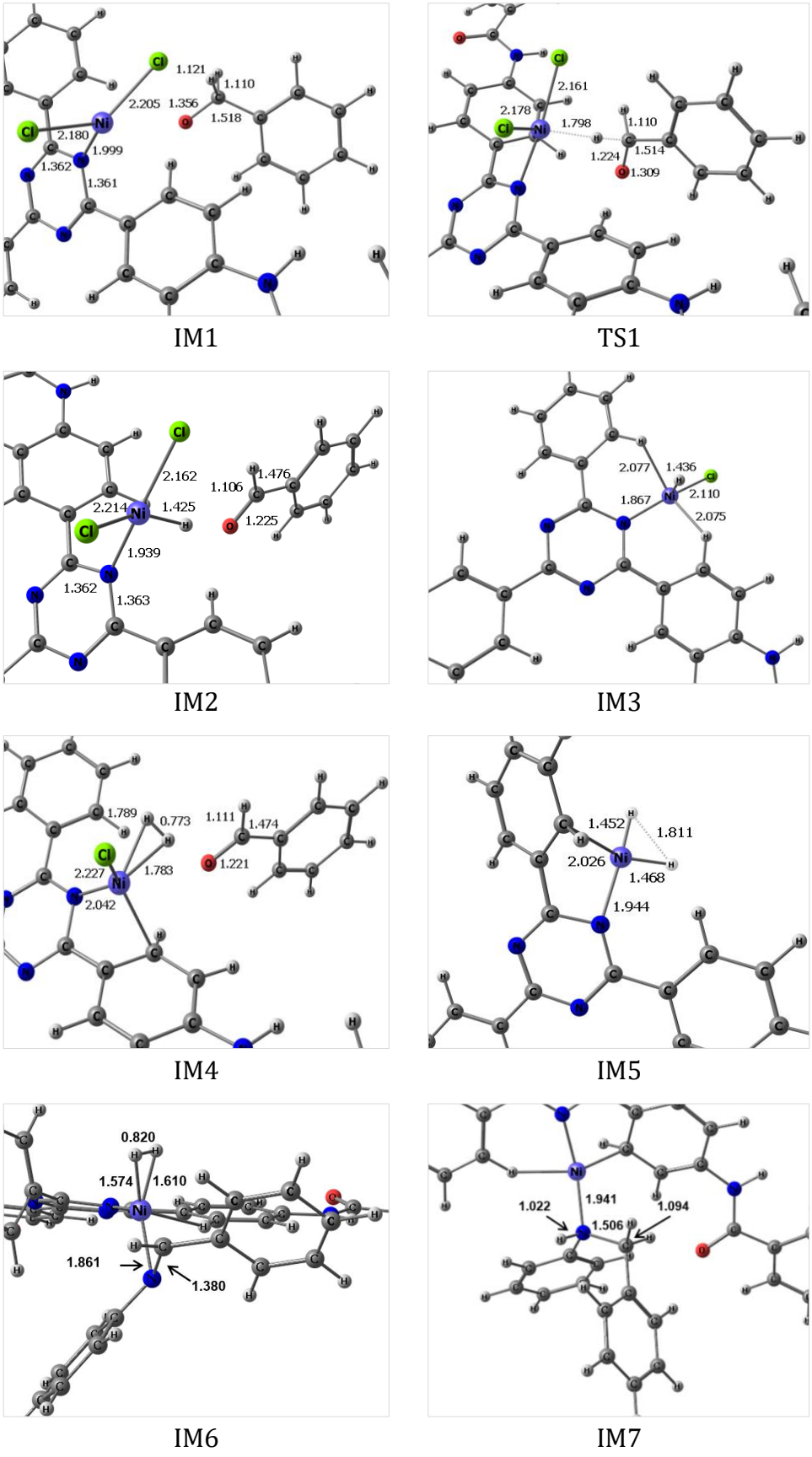

Figure 5.8 Optimized geometries of all intermediates and transition state associated with *N*-alkylation reaction over MOP-Am2-m at B3LYP/6-31G(d) level of theory

In IM1, one benzyl alcohol interacts with Ni(II) *via* 1a configuration that results in the interaction energy of –20.47 kcal/mol. Upon interaction with benzyl alcohol, the Ni–Cl bond length elongates (2.159 Å to 2.205 Å; 2.155 Å to 2.180 Å) as well as that of Ni–N bond length (1.936 Å to 1.999 Å). The reaction proceeds further when one H atom from benzylic position migrated towards Ni(II) *via* transition state, TS1. In TS1, elongation of C–H bond length (1.121 Å to 1.224 Å) and formation of new Ni–H bond (1.798 Å) take place which indicates transfer of H atom from α-carbon to Ni(II). The barrier height for this step is 24.82 kcal/mol and TS is validated from the presence of one imaginary frequency, **301*i***. IM2 depicts a strong Ni–H bond formation as expected from bond length value (1.425 Å). Simultaneous shortening of C–O bond (1.309 Å to 1.225 Å) confirms the formation of benzaldehyde from the reactant molecule. The presence of aniline in the solution eventually reacts with the generated benzaldehyde to form an imine intermediate. IM2 is energetically –23.78 kcal/mol lower than the starting material which indicates that the *H*-abstraction step is exothermic by 3.30 kcal/mol. Subsequently, one Cl^- ion and benzaldehyde are removed from the system, forming IM3. In IM3, Ni–H bond length was 1.436 Å and Ni–Cl bond length was 2.110 Å. IM3 is -49.35 kcal/mol lower in energy with respect to the starting point.

Another benzoxide enters the system which again give away its benzylic H to Ni(II), that eventually forming H_2 molecule which is evident from its bond length (0.773 Å). This step is quite facile as addition of second H atom into the metal ion is easily achieved without any energy barrier. After that, IM5 is formed when one more Cl^- ion and benzaldehyde are removed from the system to the solution. It is evident from the potential energy diagram (PES) that IM4 and IM5 are stabilized by –91.00 kcal/mol and –95.90 kcal/mol, respectively. Looking into the energies of intermediates and transition state, the overall reaction path is exothermic.

In the meantime, the amine present in the solution starts reacting with the generated benzaldehyde forming imine intermediate. IM5 starts interacting with the imine intermediate for hydrogenation. IM6 denotes the interaction of incoming imine towards the catalyst NiH_2 stabilized by –100.96 kcal/mol. The hydrogenation on the imine intermediate by NiH_2 elongates the C=N bond length from 1.380 Å to 1.506 Å.

This is attributed to the formation of C–N bond with relative stabilization energy of –103.12 kcal/mol. It is denoted by IM7 which finally gives the product.

Based on the potential energy surface (PES) the best probable mechanism involved in *N*-alkylation is shown in Figure 5.9.

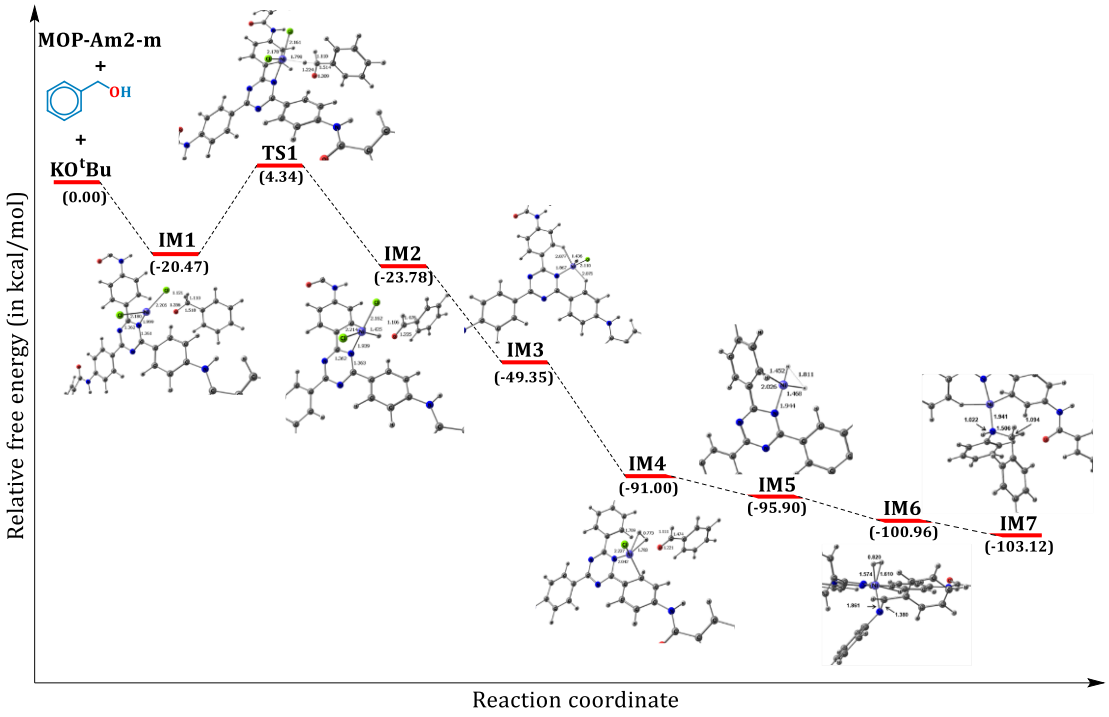

Figure 5.9 Potential energy surface (PES) diagram of *N*-alkylation reaction

Once the desired product is formed *via* reductive elimination, the oxidation state of Ni changes from +2 to 0. The presence of Cl^- in the reaction medium eventually coordinates with the metal ion stabilizing the oxidation state to its original form and allowing the catalyst for further reaction cycles.

5.2.6 Catalyst reusability and stability

The major concern about a heterogeneous catalyst in any domain of reactions is recyclability and efficiency. The recyclability of Ni@MOP-Am2 was examined for the production of **66b**. Interestingly four consecutive cycles showed comparable results while for the 5th cycle, the productivity was decreased drastically (Figure 5.10a). The reused catalyst was recovered after the 5th catalytic cycle and characterized with PXRD analysis. Besides having undisturbed structural integrity, the 2θ value at 16.09° has now shifted to 15.74° which is a characteristic signal of MOP-Am2 (Figure

5.10b). This outcome might be responsible for the leaching of Ni(II) which is responsible for decreasing the conversion yield.

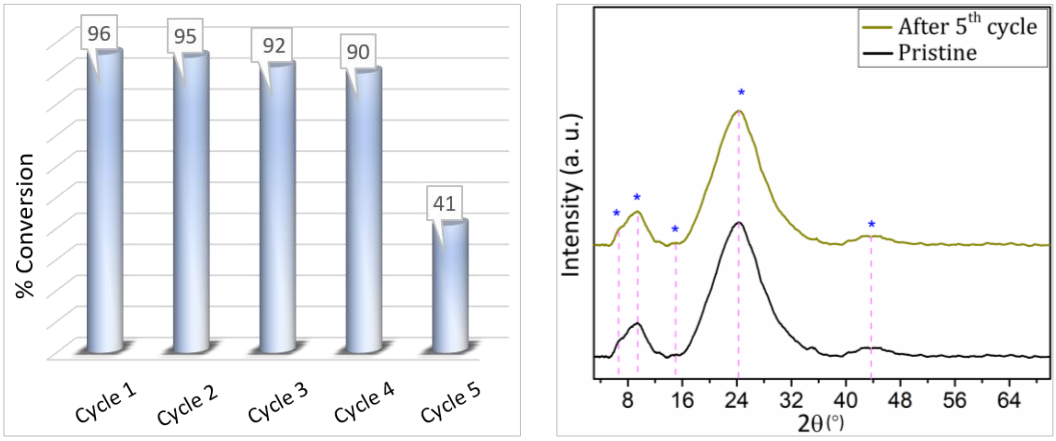

(a) (b)

Figure 5.10 (a) Five catalytic reusability cycle and (b) overlay PXRD spectra of reused Ni@MOP-Am2

5.3 Summary

The enriched nitrogen in the amide functionalized trazine porous organic polymer behaves as a scaffold for metal immobilization. The catalytic potency of the Ni(II) embedded Ni@MOP-Am2 is demonstrated with base mediated *N*-alkylation reaction from diverse alcohols and amines *via* borrowing hydrogen strategy. The protocol affirmed good to excellent yield and easy catalyst recovery up to 5th cycle. Computational study suggested a three-step combined mechanism. At first the alcohol is oxidized to its corresponding carbonyl compound under anaerobic condition leaving H_2 which was trapped by the Ni(II) ion present on the support catalyst in the reaction media, followed by the Schiff-base condensation of the carbonyl compound and amine to form imine intermediate in the second step. The third step is the *in-situ* reduction of C=N by the captured H_2 on the catalyst. This process of transfer of H_2 is known as "hydrogen autotransfer".

5.4 Experimental Section

5.4.1 Materials and methods

All the chemicals employed are brought from commercial sources (Sigma Aldrich, Alfa Aesar and Merck) and were used as such without further purification until

otherwise mentioned. FT-IR spectra were recorded in the range 4000-500 cm^{-1} by preparing the sample pellets in KBr using Perkin Elmer spectrophotometer.

The powder X-ray diffraction (PXRD) was recorded in D8 ADVANCE X-ray using monochromated Cu Kα (λ = 1.542 Å) radiation made by Bruker. Thermogravimetric analyses (TGA) were performed on a Shimadzu 60 thermal analyzer at a heating rate of 10 °C min^{-1} under continuous nitrogen flow. The porosity and rigidity of MOP-Am2 has been measured recording the N_2 adsorption-desorption isotherm of it at Quantachrome (Version 3.0) surface area analyzer. The liquid nitrogen used in the measurement was of ultra-high purity (99.999% pure) and the refrigerated bath of liquid nitrogen (77 K) further controls the temperature during the process.

Atomic absorption spectrophotometer measurement was recorded in Thermo ICE 3500 series, coupled with a hydride vapour generator, VP100. X-ray photoelectron spectroscopy (XPS) measurement was carried out using a Thermo-Scientific ESCALAB Xi+ spectrometer with a monochromatic Al Kα X-ray source (1486.6 eV) and a spherical energy analyzer that operates in the CAE (constant analyzer energy) mode. The CAE for the survey spectrum is 200 eV and for high-resolution spectra is 50 eV.

Field emission scanning electron microscope (FESEM) images were recorded in Gemini 500 FESEM (software: SmartSEm User Interface). Transmission electron microscope (TEM) images and TEM-EDX spectrum were recorded in JEOL JEM 2100 at an accelerating voltage of 200 kV to examine the surface and bulk morphology.

The progress of the reactions was monitored by TLC using TLC silica gel F254 250 μm precoated-plates from Merck and the product formation was confirmed by NMR spectrometer (Bruker AVANCE NEO NMR SPECT. 400 MHz), (JEOL ECS-400, DELTA, VERSION-4.3.6), (Bruker, AVANCE III HD 600 MHz), HRMS (Xevo G2-XS QTof (Waters) mass spectrometer using electron spray ionization mass) and GCMS analysis from Perkin Elmer using Turbomass-VER software.

5.4.2 Synthesis of Ni@MOP-Am2

The construct the Ni@MOP-Am2; a reported procedure had been followed as discussed in Chapter 4 to synthesize MOP-Am2. 100 mg of the obtained pale yellow

powdery material was then dispersed in 20 mL of dichloromethane (DCM) and continued stirring with 10% of $NiCl_2 \cdot 6H_2O$ at room temperature for 24 h. The residue was then filtered and washed thoroughly with water to avoid unreacted Ni(II)-salt. The precipitate of the desired product was dried under vacuum at 100 °C for 24 h to remove the surface captured solvent molecules and then characterized.

5.4.3 General synthetic procedure for *N*-alkylation of amines with alcohols

In a 20 mL Schlenk tube 1.1 mmol of alcohols, 0.5 mmol of amines, 0.4 mmol of KO^tBu, 15 wt% of Ni@MOP-Am, and 1-2 mL of toluene were added and heated at 120 °C for 18-26 h. The reactions are monitored using TLC. The desired products were isolated by column chromatography using varied ethyl acetate:*n*-hexane mixture. The isolated products were characterized by ^1H and ^{13}C NMR spectroscopy and HRMS.

5.4.4 Single crystal X-ray diffraction

Yellowish needle and block shaped crystals of **66o** and **69f** were observed in chloroform. Single crystal X-ray diffractions were collected on a Bruker SMART APEX-II CCD diffractometer using Mo Kα (λ =0.71073 Å) radiation. Bruker-SAINT software was employed for reducing the data and SADABS for correcting intensity absorption. Structures were solved and refined using SHELXL with anisotropic displacement parameters for non-H atoms. C–H atoms were fixed geometrically using the HFIX command in SHELX-TL. PLATON was used for correction in error for missing symmetry.

5.4.5 Computational details

Gaussian 09 software package is used to perform Density Functional Theory (DFT) calculations to obtain the geometry optimizations, ground state energies and vibrational frequencies of the species in interest [39]. A popular and dependable Becke-3-parameter-Lee-Yang-Parr B3LYP functional along with 6-31G(d) basis set is chosen for the geometry optimizations. Presence of only one imaginary frequency in the vibrational spectra confirms the transition states, whereas, no imaginary frequency is observed for the reactant, intermediates, and products, confirming that they are true minima. Berny algorithm is carried out for the geometry optimization of a transition state structure [40].

5.5 Spectral data analysis

***N-(4-methylbenzyl)aniline*:**

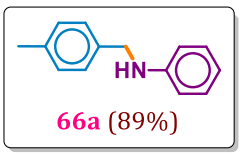

^{1}H NMR (400 MHz, $CDCl_3$) δ (ppm): 7.32 (d, *J* = 8.0 Hz, 2H), 7.25–7.21 (m, 3H), 6.81–6.76 (m, 1H), 6.71–6.67 (m, 4H), 4.33 (s, 2H), 4.02 (s, 1H), 2.41 (s, 3H). ^{13}C{^{1}H} NMR (101 MHz, $CDCl_3$) δ (ppm): 148.4, 137.0, 136.5, 129.5, 129.4, 127.7, 117.6, 113.0, 48.2, 21.1. HRMS (ESI-TOF) m/z: $[M+H]^+$ calcd for $C_{14}H_{16}N$ is 198.1282; found 198.1286.

***4-methyl-N-(4-methylbenzyl)aniline*:**

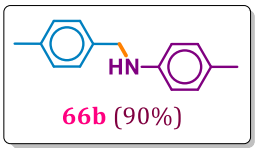

^{1}H NMR (400 MHz, $CDCl_3$) δ (ppm): 7.24 (d, *J* = 8.0 Hz, 2H), 7.13 (d, *J* = 7.8 Hz, 2H), 6.97 (d, *J* = 8.0 Hz, 2H), 6.56–6.53 (m, 2H), 4.24 (s, 2H), 3.83 (s, 1H), 2.33 (s, 3H), 2.23 (s, 3H). ^{13}C{^{1}H} NMR (101 MHz, $CDCl_3$) δ (ppm): 146.2, 136.9, 136.7, 129.9, 129.4, 127.7, 126.8, 113.1, 48.5, 21.3, 20.6. HRMS (ESI-TOF) m/z: $[M+H]^+$ calcd for $C_{15}H_{18}N$ is 212.1439; found 212.1434.

***4-methoxy-N-(4-methylbenzyl)aniline*:**

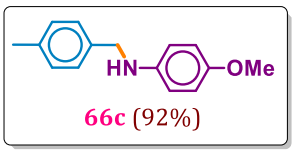

^{1}H NMR (400 MHz, $CDCl_3$) δ (ppm): 7.25 (d, *J* = 8.1 Hz, 2H), 7.14 (d, *J* = 7.9 Hz, 2H), 6.80–6.74 (m, 2H), 6.63–6.57 (m, 2H), 4.23 (s, 2H), 3.73 (s, 3H), 2.34 (s, 3H). ^{13}C{^{1}H} NMR (101 MHz, $CDCl_3$) δ (ppm): 152.3, 142.7, 137.0, 136.7, 129.4, 127.7, 115.0, 114.2, 55.9, 49.1, 21.3. HRMS (ESI-TOF) m/z: $[M+H]^+$ calcd for $C_{15}H_{18}NO$ is 228.1388; found 228.1382.

***4-butyl-N-(4-methylbenzyl)aniline*:**

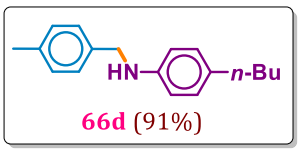

^{1}H NMR (400 MHz, $CDCl_3$) δ (ppm): 7.30 (d, *J* = 8.0 Hz, 2H), 7.19 (d, *J* = 7.8 Hz, 2H), 7.09–6.98 (m, 2H), 6.66–6.59 (m, 2H), 4.30 (s, 2H), 2.55 (t, *J* = 7.6 Hz, 2H), 2.39 (s, 3H), 1.63–1.56 (m, 2H), 1.40 (dt, *J* = 14.5, 7.3 Hz, 2H), 0.97 (t, *J* = 7.3 Hz, 3H). ^{13}C{^{1}H} NMR (101 MHz, $CDCl_3$) δ (ppm): 146.3, 136.9, 136.8, 132.2, 129.4, 127.7, 113.1, 48.6, 34.9, 34.2, 22.5, 21.3, 14.2. HRMS (ESI-TOF) m/z: $[M+H]^+$ calcd for $C_{18}H_{24}N$ is 254.1908; found 254.1902.

***3,5-dimethyl-N-(4-methylbenzyl)aniline*:**

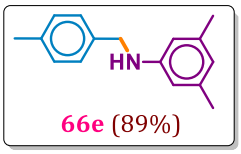

^{1}H NMR (400 MHz, $CDCl_3$) δ (ppm): 7.29 (d, *J* = 8.0 Hz, 2H), 7.18 (d, *J* = 7.8 Hz, 2H), 6.42 (s, 1H), 6.32 (s, 2H), 4.28 (s, 2H), 3.87 (s, 1H), 2.38 (s, 3H), 2.27 (s, 6H). $^{13}C\{^{1}H\}$ NMR (101 MHz, $CDCl_3$) δ (ppm): 148.6, 139.1, 137.0, 136.7, 129.4, 127.7, 119.7, 110.9, 48.3, 21.7. HRMS (ESI-TOF) m/z: $[M+H]^+$ calcd for $C_{16}H_{20}N$ is 226.1595; found 226.1594.

***2,4-dimethyl-N-(4-methylbenzyl)aniline*:**

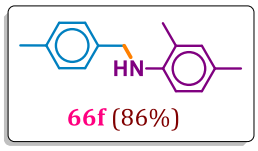

^{1}H NMR (400 MHz, $CDCl_3$) δ (ppm): 7.27 (d, *J* = 8.0 Hz, 2H), 7.15 (d, *J* = 7.8 Hz, 2H), 6.94–6.86 (m, 2H), 6.56–6.51 (m, 1H), 4.30 (s, 2H), 2.35 (s, 3H), 2.22 (s, 3H), 2.13 (s, 3H). $^{13}C\{^{1}H\}$ NMR (101 MHz, $CDCl_3$) δ (ppm): 144.1, 137.0, 136.8, 131.1, 129.5, 127.7, 127.5, 126.4, 122.2, 110.3, 48.5, 21.3, 20.5, 17.7. HRMS (ESI-TOF) m/z: $[M+H]^+$ calcd for $C_{16}H_{20}N$ is 226.1595; found 226.1594.

***4-fluoro-N-(4-methylbenzyl)aniline*:**

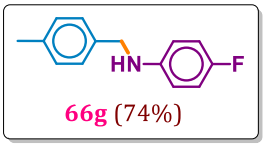

^{1}H NMR (400 MHz, $CDCl_3$) δ (ppm): 7.26 (d, *J* = 8.0, 3.0 Hz, 2H), 7.17 (d, *J* = 7.9 Hz, 2H), 6.94–6.83 (m, 2H), 6.61–6.53 (m, 2H), 4.25 (s, 2H), 3.90 (s, 1H), 2.36 (s, 3H). $^{13}C\{^{1}H\}$ NMR (101 MHz, $CDCl_3$) δ (ppm): 156.0 (d, J_{C-F} = 234.8 Hz), 144.7, 137.1, 136.3, 129.5, 127.6, 115.8 (d, J_{C-F} = 22.4 Hz), 113.8 (d, J_{C-F} = 7.6 Hz), 48.8, 21.3. HRMS (ESI-TOF) m/z: $[M+H]^+$ calcd for $C_{14}H_{15}FN$ is 216.1188; found 216.1184.

***4-chloro-N-(4-methylbenzyl)aniline*:**

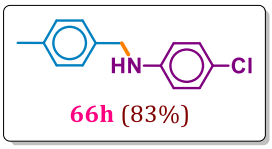

^{1}H NMR (400 MHz, $CDCl_3$) δ (ppm): 7.23 (d, *J* = 8.0 Hz, 2H), 7.15 (d, *J* = 8.2 Hz, 2H), 7.12–7.07 (m, 2H), 6.56–6.51 (m, 2H), 4.25 (s, 2H), 4.02 (s, 1H), 2.34 (s, 3H). $^{13}C\{^{1}H\}$ NMR (101 MHz, $CDCl_3$) δ (ppm): 146.9, 137.2, 136.0, 129.6, 129.3, 127.6, 122.2, 114.0, 48.3, 21.3. HRMS (ESI-TOF) m/z: $[M+H]^+$ calcd for $C_{14}H_{15}ClN$ is 232.0893; found 232.0886.

***2-chloro-N-(4-methylbenzyl)aniline*:**

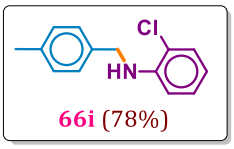

^{1}H NMR (400 MHz, $CDCl_3$) δ (ppm): 7.33–7.27 (m, 3H), 7.20 (d, *J* = 7.8 Hz, 2H), 7.13 (ddd, *J* = 8.2, 7.4, 1.5 Hz, 1H), 6.70–6.64 (m, 2H), 4.74 (s, 1H), 4.39 (s, 2H), 2.39 (s, 3H). $^{13}C\{^{1}H\}$ NMR (101 MHz,

$CDCl_3$) δ (ppm): 144.1, 137.2, 135.8, 129.6, 129.6, 129.3, 129.2, 128.0, 127.9, 127.5, 127.5, 119.3, 117.5, 111.7, 47.8, 21.3. HRMS (ESI-TOF) m/z: $[M+H]^+$ calcd for $C_{14}H_{15}ClN$ is 232.0893; found 232.088.

***3-iodo-N-(4-methylbenzyl)aniline*:**

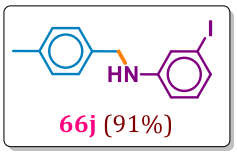

^1H NMR (400 MHz, $CDCl_3$) δ (ppm): 7.24 (d, *J* = 8.0 Hz, 2H), 7.16 (d, *J* = 8.0 Hz, 2H), 7.01 (ddd, *J* = 11.4, 2.7, 1.1 Hz, 2H), 6.86 (t, *J* = 7.9 Hz, 1H), 6.58–6.54 (m, 1H), 4.24 (s, 2H), 3.99 (s, 1H), 2.35 (s, 3H). $^{13}C\{^1H\}$ NMR (101 MHz, $CDCl_3$) δ (ppm): 149.5, 137.3, 135.8, 130.9, 129.6, 127.7, 126.5, 121.5, 112.2, 95.4, 48.0, 21.3. HRMS (ESI-TOF) m/z: $[M+H]^+$ calcd for $C_{14}H_{15}IN$ is 324.0249; found 324.0243.

***3-((4-methylbenzyl)amino)phenol*:**

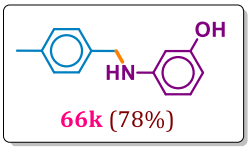

^1H NMR (400 MHz, $CDCl_3$) δ (ppm): 7.22 (d, *J* = 7.9 Hz, 2H), 7.13 (d, *J* = 7.8 Hz, 2H), 6.99 (t, *J* = 8.0 Hz, 1H), 6.23–6.14 (m, 2H), 6.10 (t, *J* = 2.2 Hz, 1H), 4.23 (s, 2H), 2.32 (s, 3H). $^{13}C\{^1H\}$ NMR (101 MHz, $CDCl_3$) δ (ppm): 156.9, 150.0, 144.8, 137.1, 136.3, 130.4, 129.5, 129.4, 127.7, 127.6, 48.2, 21.3. HRMS (ESI-TOF) m/z: $[M+H]^+$ calcd for $C_{14}H_{16}NO$ is 214.1231; found 214.1235.

1-(4-methylbenzyl)-2-phenylhydrazine:

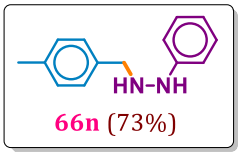

^1H NMR (400 MHz, $CDCl_3$) δ (ppm): 7.29 (d, *J* = 7.9 Hz, 2H), 7.24–7.17 (m, 4H), 6.78–6.72 (m, 1H), 6.69–6.65 (m, 2H), 4.31 (s, 2H), 4.02 (s, 1H), 2.38 (s, 3H). $^{13}C\{^1H\}$ NMR (101 MHz, $CDCl_3$) δ (ppm): 148.3, 137.0, 136.5, 129.4, 127.7, 117.6, 113.0, 48.2, 21.3. HRMS (ESI-TOF) m/z: $[M+H]^+$ calcd for $C_{14}H_{17}N_2$ is 213.1391; found 213.1284.

***4,4'-oxybis(N-(4-methylbenzyl)aniline)*:**

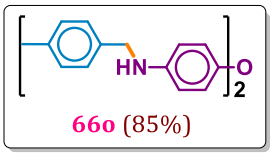

^1H NMR (400 MHz, $CDCl_3$) δ (ppm): 7.26 (d, *J* = 8.0 Hz, 2H), 7.16 (d, *J* = 7.8 Hz, 2H), 6.85–6.80 (m, 2H), 6.61–6.56 (m, 2H), 4.25 (s, 2H), 2.35 (s, 3H). $^{13}C\{^1H\}$ NMR (101 MHz, $CDCl_3$) δ (ppm): 150.2, 144.0, 137.1, 136.5, 129.4, 127.8, 119.7, 114.0, 49.0, 21.3. HRMS (ESI-TOF) m/z: $[M+H]^+$ calcd for $C_{28}H_{29}N_2O$ is 409.2279; found 409.2270.

***N-benzyl-4-methylaniline*:**

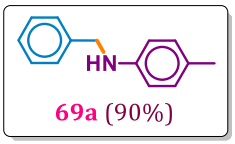

69a (90%)

^{1}H NMR (400 MHz, $CDCl_3$) δ (ppm): 7.34 (dd, *J* = 13.4, 7.3 Hz, 4H), 7.25 (t, *J* = 7.0 Hz, 1H), 6.97 (d, *J* = 8.2 Hz, 2H), 6.55 (d, *J* = 8.3 Hz, 2H), 4.29 (s, 2H), 2.23 (s, 3H). $^{13}C\{^{1}H\}$ NMR (126 MHz, $CDCl_3$) δ (ppm): 146.1, 139.8, 129.9, 128.8, 127.7, 127.3, 126.9, 113.2, 48.9, 20.6. HRMS (ESI-TOF) m/z: $[M+H]^+$ calcd for $C_{14}H_{16}N$ is 198.1282; found 198.1287.

***N-(4-methoxybenzyl)-4-methylaniline*:**

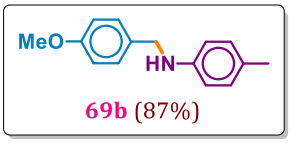

69b (87%)

^{1}H NMR (400 MHz, $CDCl_3$) δ (ppm): 7.30–7.26 (m, 2H), 6.98 (d, *J* = 8.0 Hz, 2H), 6.89–6.85 (m, 2H), 6.58–6.54 (m, 2H), 4.22 (s, 2H), 3.79 (s, 3H), 2.23 (s, 3H). $^{13}C\{^{1}H\}$ NMR (101 MHz, $CDCl_3$) δ (ppm): 159.0, 146.2, 131.8, 129.9, 129.0, 126.9, 114.2, 113.2, 55.5, 48.3, 20.6. HRMS (ESI-TOF) m/z: $[M+H]^+$ calcd for $C_{15}H_{18}NO$ is 228.1388; found 228.1381.

***N-(4-chlorobenzyl)-4-methylaniline*:**

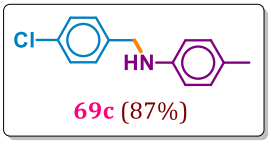

69c (87%)

^{1}H NMR (400 MHz, $CDCl_3$) δ (ppm): 7.30 (s, 4H), 7.01–6.97 (m, 2H), 6.56–6.52 (m, 2H), 4.29 (s, 2H), 2.24 (s, 3H). $^{13}C\{^{1}H\}$ NMR (101 MHz, $CDCl_3$) δ (ppm): 145.7, 138.4, 132.9, 130.0, 128.9, 128.8, 127.2, 113.2, 48.1, 20.6. HRMS (ESI-TOF) m/z: $[M+H]^+$ calcd for $C_{14}H_{15}ClN$ is 232.0893; found 232.0897.

***N-butyl-4-methylaniline*:**

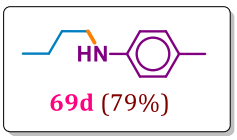

69d (79%)

^{1}H NMR (400 MHz, $CDCl_3$) δ (ppm): 6.98 (d, *J* = 8.1 Hz, 2H), 6.57–6.51 (m, 2H), 3.09 (t, *J* = 7.2 Hz, 2H), 2.23 (s, 3H), 1.62–1.56 (m, 2H), 1.47–1.37 (m, 2H), 0.95 (t, *J* = 7.3 Hz, 3H). $^{13}C\{^{1}H\}$ NMR (101 MHz, $CDCl_3$) δ (ppm): 146.5, 129.9, 126.5, 113.1, 44.3, 31.9, 20.6, 20.5, 14.1. HRMS (ESI-TOF) m/z: $[M+H]^+$ calcd for $C_{11}H_{18}N$ is 164.1439; found 164.1442.

***4-methyl-N-(naphthalen-1-ylmethyl)aniline*:**

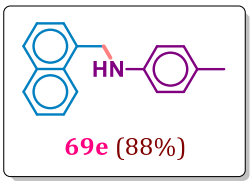

69e (88%)

^{1}H NMR (400 MHz, $CDCl_3$) δ (ppm): 8.13–8.08 (m, 1H), 7.94–7.90 (m, 1H), 7.83 (d, *J* = 8.2 Hz, 1H), 7.58–7.43 (m, 4H), 7.08–7.03 (m, 2H), 6.67–6.62 (m, 2H), 4.74 (s, 2H), 2.30 (s, 3H). $^{13}C\{^{1}H\}$ NMR (101 MHz, $CDCl_3$) δ (ppm): 146.2, 134.7, 134.0, 131.7, 130.0, 128.9, 128.3, 126.9, 126.5, 126.1, 126.0, 125.7, 123.8, 113.0, 46.9, 20.6. HRMS (ESI-TOF) m/z: $[M+H]^+$ calcd for $C_{18}H_{18}N$ is 248.1439; found 248.1433.

***N-benzhydryl-4-methylaniline*:**

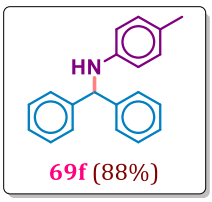

^{1}H NMR (400 MHz, $CDCl_3$) δ (ppm): 7.53–7.23 (m, 10H), 6.97 (d, *J* = 7.1 Hz, 2H), 6.51 (d, *J* = 6.7 Hz, 2H), 5.51 (s, 1H), 4.15 (s, 1H), 2.25 (s, 3H). ^{13}C{^{1}H} NMR (101 MHz, $CDCl_3$) δ (ppm): 145.3, 143.3, 129.8, 128.9, 127.6, 127.4, 126.9, 113.8, 63.5, 20.5. HRMS (ESI-TOF) m/z: $[M+H]^+$ calcd for $C_{20}H_{20}N$ is 274.1595; found 274.1590.

5.6 Bibliography

[1] Irrgang, T. and Kempe, R. Transition-metal-catalyzed reductive amination employing hydrogen. *Chemical Reviews*, 120(17):9583-9674, 2020.

[2] Murugesan, K., Senthamarai, T., Chandrashekhar, V. G., Natte, K., Kamer, P. C., Beller, M., and Jagadeesh, R. V. Catalytic reductive aminations using molecular hydrogen for synthesis of different kinds of amines. *Chemical Society Reviews*, 49(17):6273-6328, 2020.

[3] Afanasyev, O. I., Kuchuk, E., Usanov, D. L., and Chusov, D. Reductive amination in the synthesis of pharmaceuticals. *Chemical Reviews*, 119(23):11857-11911, 2019.

[4] Bariwal, J. and Van der Eycken, E. C–N bond forming cross-coupling reactions: an overview. *Chemical Society Reviews*, 42(24):9283-9303, 2013.

[5] Saikia, R., Boruah, P. K., Ahmed, S. M., Das, M. R., Thakur, A. J., and Bora, U. An avenue to Chan-Lam *N*-arylation by Cu (0) nanoparticles immobilized graphitic carbon-nitride oxide surface. *Applied Catalysis A: General*, 643:118767, 2022.

[6] Surry, D. S. and Buchwald, S. L. Diamine ligands in copper-catalyzed reactions. *Chemical Science*, 1(1):13-31, 2010.

[7] Hassan, J., Sévignon, M., Gozzi, C., Schulz, E., and Lemaire, M. Aryl–aryl bond formation one century after the discovery of the Ullmann reaction. *Chemical Reviews*, 102(5):1359-1470, 2022.

[8] Yamaguchi, A., Sato, O., Mimura, N., and Shirai, M. Catalytic production of sugar alcohols from lignocellulosic biomass. *Catalysis Today*, 265:199-202, 2016.

[9] Barta, K. and Ford, P. C. Catalytic conversion of nonfood woody biomass solids to organic liquids. *Accounts of Chemical Research*, 47(5):1503-1512, 2014.

[10] Edwards, M. G., Jazzar, R. F., Paine, B. M., Shermer, D. J., Whittlesey, M. K., Williams, J. M. J., and Edney, D. D. Borrowing hydrogen: a catalytic route to C–C bond formation from alcohols. *Chemical Communications*, (1):90-91, 2004.

[11] Reed-Berendt, B. G., Latham, D. E., Dambatta, M. B., and Morrill, L. C. Borrowing hydrogen for organic synthesis. *ACS Central Science*, 7(4):570-585, 2021.

[12] Luo, N., Zhong, Y., Wen, H., and Luo, R. Cyclometalated Iridium complex-catalyzed *N*-alkylation of amines with alcohols *via* borrowing hydrogen in aqueous media. *ACS Omega*, 5(42):27723-27732, 2020.

[13] Enyong, A. B. and Moasser, B. Ruthenium-catalyzed *N*-alkylation of amines with alcohols under mild conditions using the borrowing hydrogen methodology. *The Journal of Organic Chemistry*, 79(16):7553-7563, 2014.

[14] Gunanathan, C. and Milstein, D. Applications of acceptorless dehydrogenation and related transformations in chemical synthesis. *Science*, 341(6143):1229712, 2013.

[15] Bauer, I. and Knölker, H. J. Iron catalysis in organic synthesis. *Chemical Reviews*, 115(9):3170-3387, 2015.

[16] Wu, P. Y., Lu, G. P., and Cai, C. Synthesis of an Fe–Pd bimetallic catalyst for *N*-alkylation of amines with alcohols *via* a hydrogen auto-transfer methodology. *Green Chemistry*, 23(1):396-404, 2021.

[17] Yan, T., Feringa, B. L., and Barta, K. Benzylamines *via* iron-catalyzed direct amination of benzyl alcohols. *ACS Catalysis*, 6(1):381-388, 2016.

[18] Rösler, S., Ertl, M., Irrgang, T., and Kempe, R. Cobalt-catalyzed alkylation of aromatic amines by alcohols. *Angewandte Chemie International Edition*, 54(50):15046-15050, 2015.

[19] Elangovan, S., Neumann, J., Sortais, J. B., Junge, K., Darcel, C., and Beller, M. Efficient and selective *N*-alkylation of amines with alcohols catalysed by manganese pincer complexes. *Nature Communications*, 7(1):12641, 2016.

[20] Chakraborty, S., Daw, P., Ben David, Y., and Milstein, D. Manganese-catalyzed α-alkylation of ketones, esters, and amides using alcohols. *ACS Catalysis*, 8(11):10300-10305, 2018.

[21] Bains, A. K., Kundu, A., Yadav, S., and Adhikari, D. Borrowing hydrogen-mediated *N*-alkylation reactions by a well-defined homogeneous nickel catalyst. *ACS Catalysis*, 9(10):9051-9059, 2019.

[22] Ghosh, I., Khamrai, J., Savateev, A., Shlapakov, N., Antonietti, M., and König, B. Organic semiconductor photocatalyst can bifunctionalize arenes and heteroarenes. *Science*, 365(6451):360-366, 2019.

[23] Alandini, N., Buzzetti, L., Favi, G., Schulte, T., Candish, L., Collins, K. D., and Melchiorre, P. Amide synthesis by Nickel/photoredox-catalyzed direct carbamoylation of (hetero) aryl bromides. *Angewandte Chemie*, 132(13):5286-5291, 2020.

[24] Vellakkaran, M., Singh, K., and Banerjee, D. An efficient and selective nickel-catalyzed direct *N*-alkylation of anilines with alcohols. *ACS Catalysis*, 7(12):8152-8158, 2017.

[25] Afanasenko, A., Elangovan, S., Stuart, M. C., Bonura, G., Frusteri, F., and Barta, K. Efficient nickel-catalysed *N*-alkylation of amines with alcohols. C*atalysis Science & Technology*, 8(21):5498-5505, 2018.

[26] Alonso, F., Riente, P., and Yus, M. Hydrogen-transfer reductive amination of aldehydes catalysed by nickel nanoparticles. *Synlett*, 2008(09):1289-1292, 2008.

[27] Gonçalves, R. S., de Oliveira, A. B., Sindra, H. C., Archanjo, B. S., Mendoza, M. E., Carneiro, L. S., Buarque, C. D., and Esteves, P. M. Heterogeneous catalysis by covalent organic frameworks (COF):$Pd(OAc)_2$@COF-300 in cross-coupling reactions. *ChemCatChem*, 8(4):743-750, 2016.

[28] Han, J., Sun, X., Wang, X., Wang, Q., Hou, S., Song, X., Wei, Y., Wang, R., and Ji, W. Covalent organic framework as a heterogeneous ligand for the regioselective oxidative Heck reaction. *Organic letters*, 22(4):1480-1484, 2020.

[29] Han, Y., Zhang, M., Zhang, Y. Q., and Zhang, Z. H. Copper immobilized at a covalent organic framework: an efficient and recyclable heterogeneous catalyst for the Chan–Lam coupling reaction of aryl boronic acids and amines. *Green Chemistry*, 20(21):4891-4900, 2018.

[30] Khatioda, R., Pathak, D., and Sarma, B. Cu (II) Complex onto a pyridine-based porous organic polymer as a heterogeneous catalyst for nitroarene reduction. *ChemistrySelect*, 3(23):6309-6320, 2018.

[31] Jati, A., Dey, K., Nurhuda, M., Addicoat, M. A., Banerjee, R. and, Maji, B. Dual metalation in a two-dimensional covalent organic framework for

photocatalytic C–N cross-coupling reactions. *Journal of the American Chemical Society*, 144(17):7822-7833, 2022.

[32] Liu, Q., Yang, S., Repich, H., Zhai, Y., Xu, X., Liang, Y., Li, H., Wang, H., and Xu, F. Porous functionalized covalent-triazine frameworks for enhanced adsorption toward polysulfides in Li–S batteries and organic dyes. *Frontiers in Chemistry*, 8:584204, 2020.

[33] Zhu, Y., Qiao, M., Peng, W., Li, Y., Zhang, G., Zhang, F., Li, Y., and Fan, X. Rapid exfoliation of layered covalent triazine-based frameworks into *N*-doped quantum dots for the selective detection of Hg^{2+} ions. *Journal of Materials Chemistry A*, 5(19):9272-9278, 2017.

[34] Ma, S., Li, Z., Jia, J., Zhang, Z., Xia, H., Li, H., Chen, X., Xu, Y., and Liu, X. Amide-linked covalent organic frameworks as efficient heterogeneous photocatalysts in water. *Chinese Journal of Catalysis*, 42(11):2010-2019, 2021.

[35] Li, D., Cen, B., Fang, C., Leng, X., Wang, W., Wang, Y., Chen, J., and Luo, M. High performance cobalt nanoparticle catalysts supported by carbon for ozone decomposition: the effects of the cobalt particle size and hydrophobic carbon support. *New Journal of Chemistry*, 45(2):561-568, 2021.

[36] Liu, J., Li, J., Ye, R., Yan, X., Wang, L., and Jian, P. Versatile bifunctional nitrogen-doped porous carbon derived from biomass in catalytic reduction of 4-nitrophenol and oxidation of styrene. *Chinese Journal of Catalysis*, 41(8):1217-1229, 2020.

[37] Wang, N., Liu, J., Zhang, M., Wang, C., Li, X., and Ma, L. Non-noble nickel-modified covalent organic framework for partial hydrogenation of aromatic terminal alkynes. *ACS Applied Materials & Interfaces*, 13(50):60135-60143, 2021.

[38] Rojas-Buzo, S., Concepción, P., Corma, A., Moliner, M., and Boronat, M. *In-Situ*-generated active Hf-hydride in zeolites for the tandem *N*-alkylation of amines with benzyl alcohol. *ACS Catalysis*, 11(13):8049-8061, 2021.

[39] Frisch, M. J., Trucks, G. W., Schlegel, H. B., Scuseria, G. E., Robb, M., Cheeseman, J. R., Scalmani, G., Barone, V., Mennucci, B., Petersson, G. A., and Nakatsuji, H. Gaussian 09, revision D.01; Gaussian Inc., Wallingford CT, 2009.

[40] Schlegel, H. B. Optimization of equilibrium geometries and transition structures. *Journal of computational chemistry*, 3(2):214-218, 1982.

5.7 Representative Spectra

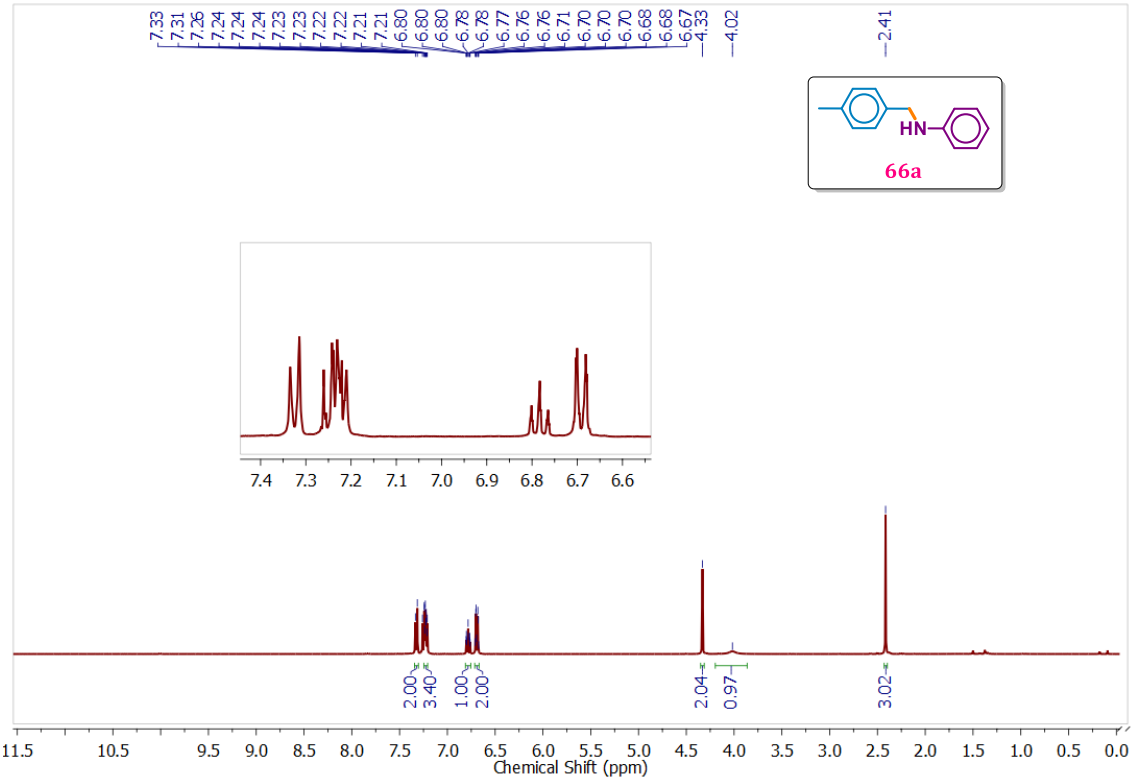

Figure 5.11 ^{1}H NMR (400 MHz, $CDCl_3$, 298 K) of **66a**

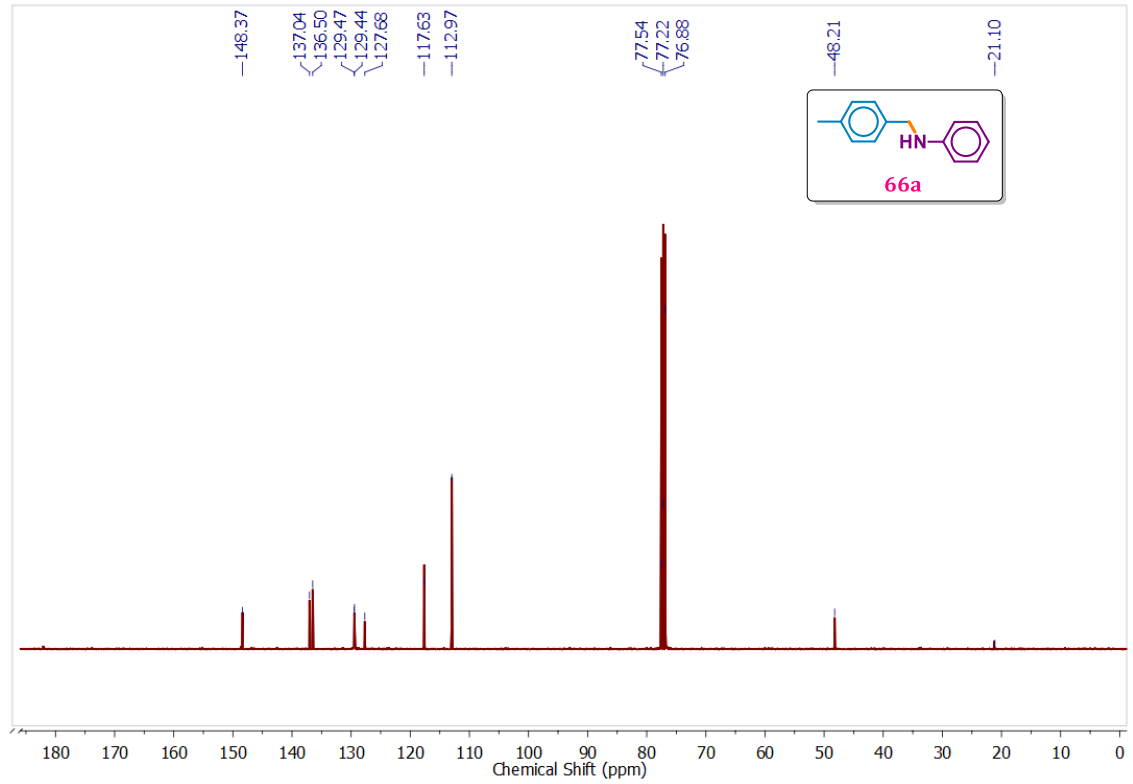

Figure 5.12 $^{13}C\{^{1}H\}$ NMR (101 MHz, $CDCl_3$, 298 K) of **66a**

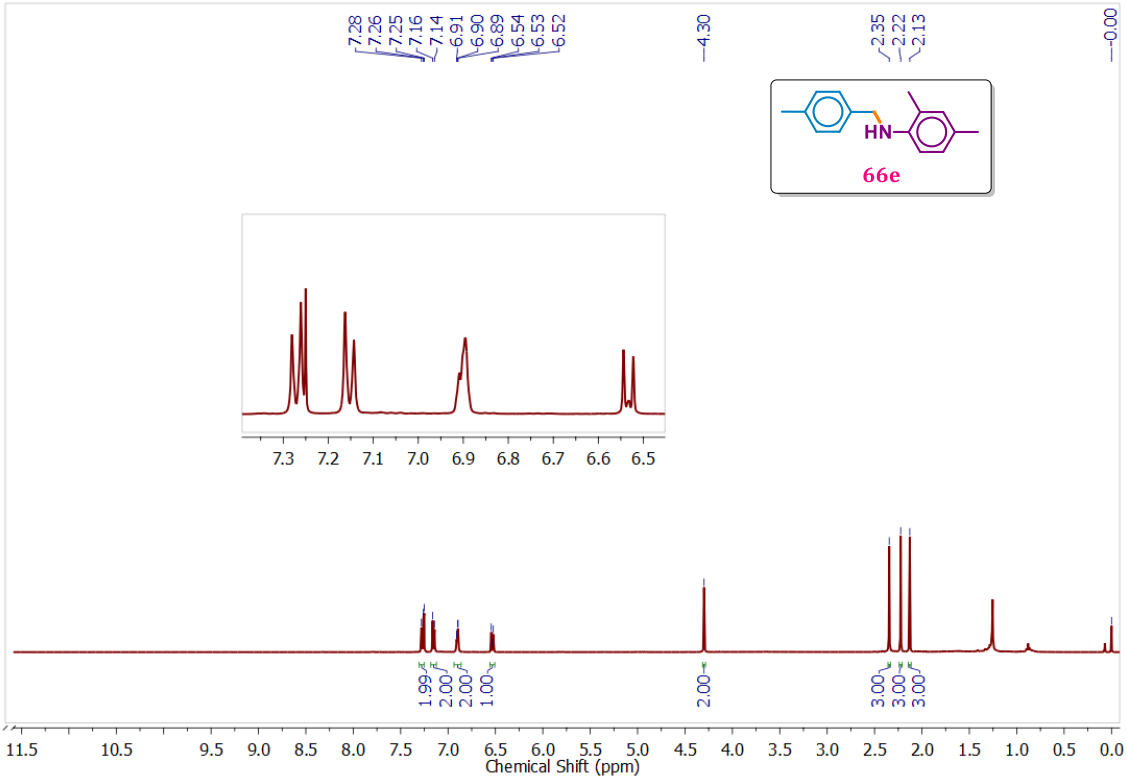

Figure 5.13 ^{1}H NMR (400 MHz, $CDCl_3$, 298 K) of **66e**

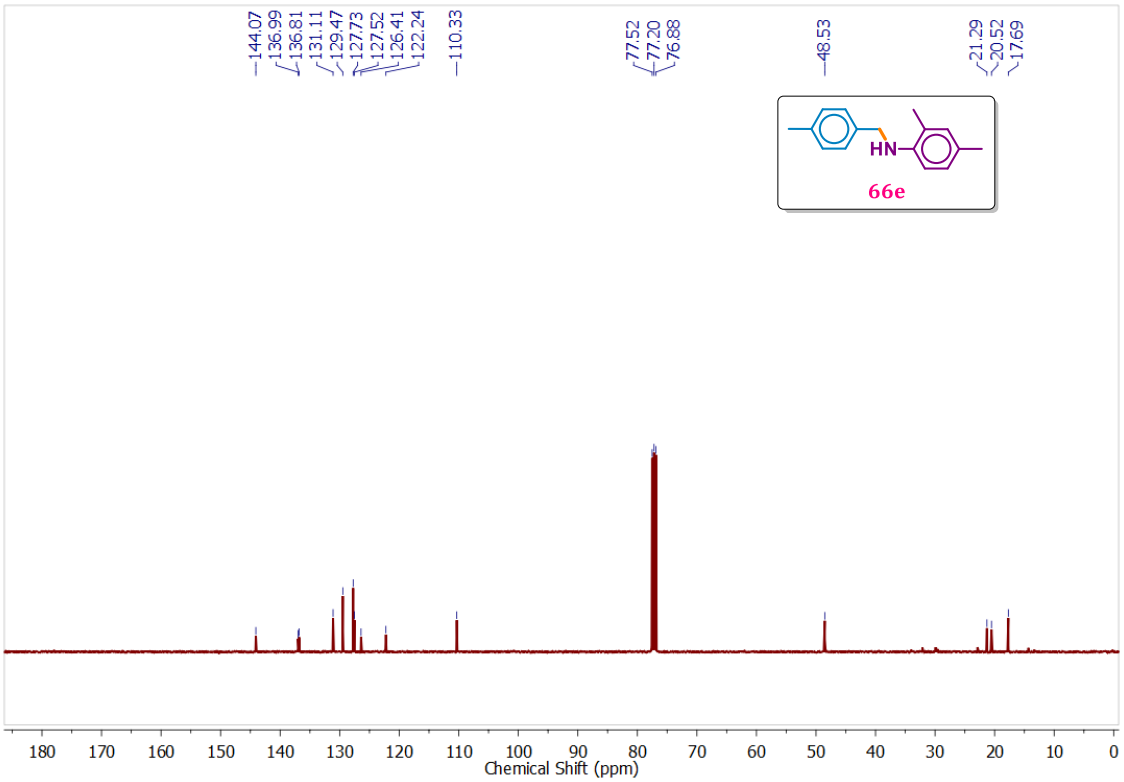

Figure 5.14 $^{13}C\{^{1}H\}$ NMR (101 MHz, $CDCl_3$, 298 K) of **66e**

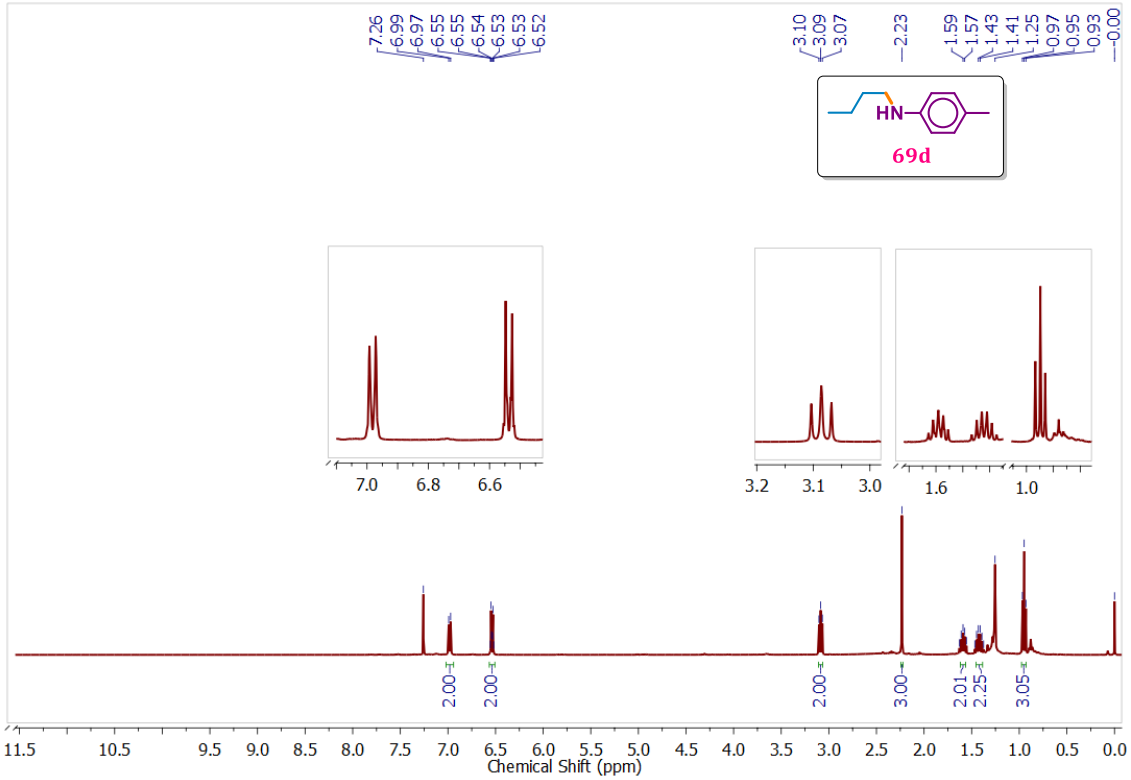

Figure 5.15 ^{1}H NMR (400 MHz, $CDCl_3$, 298 K) of **69d**

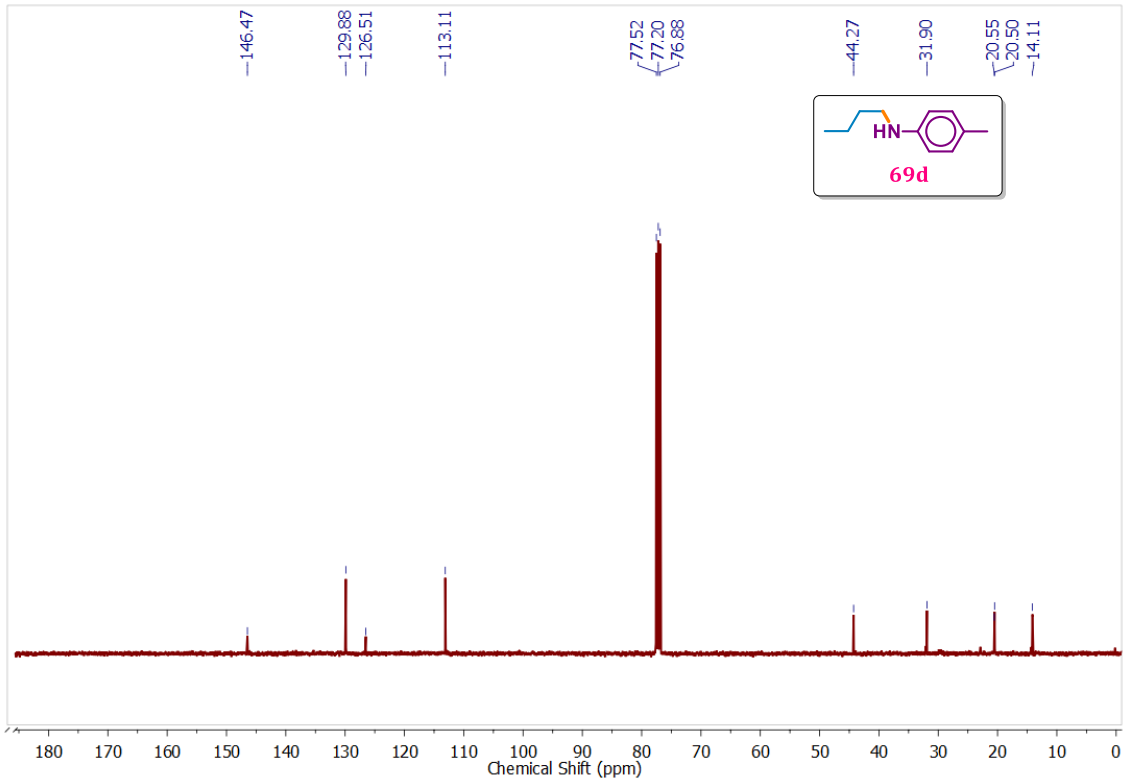

Figure 5.16 $^{13}C\{^{1}H\}$ NMR (101 MHz, $CDCl_3$, 298 K) of **69d**

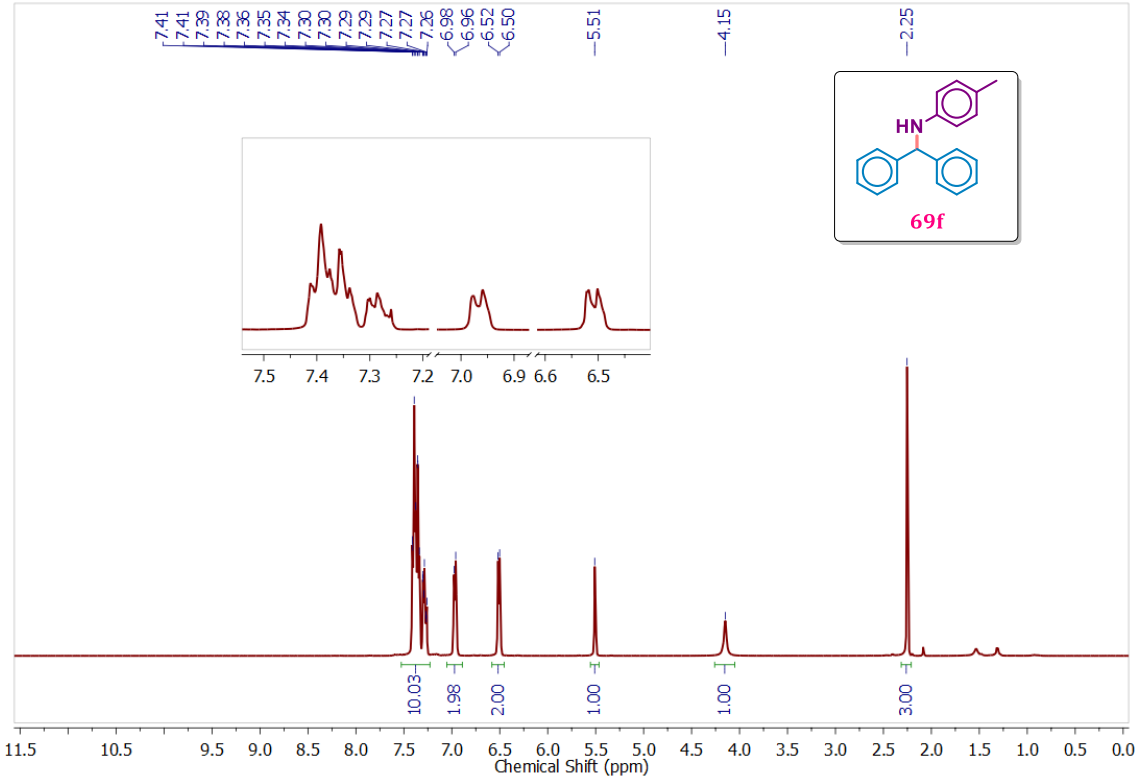

Figure 5.17 ^{1}H NMR (400 MHz, $CDCl_3$, 298 K) of **69f**

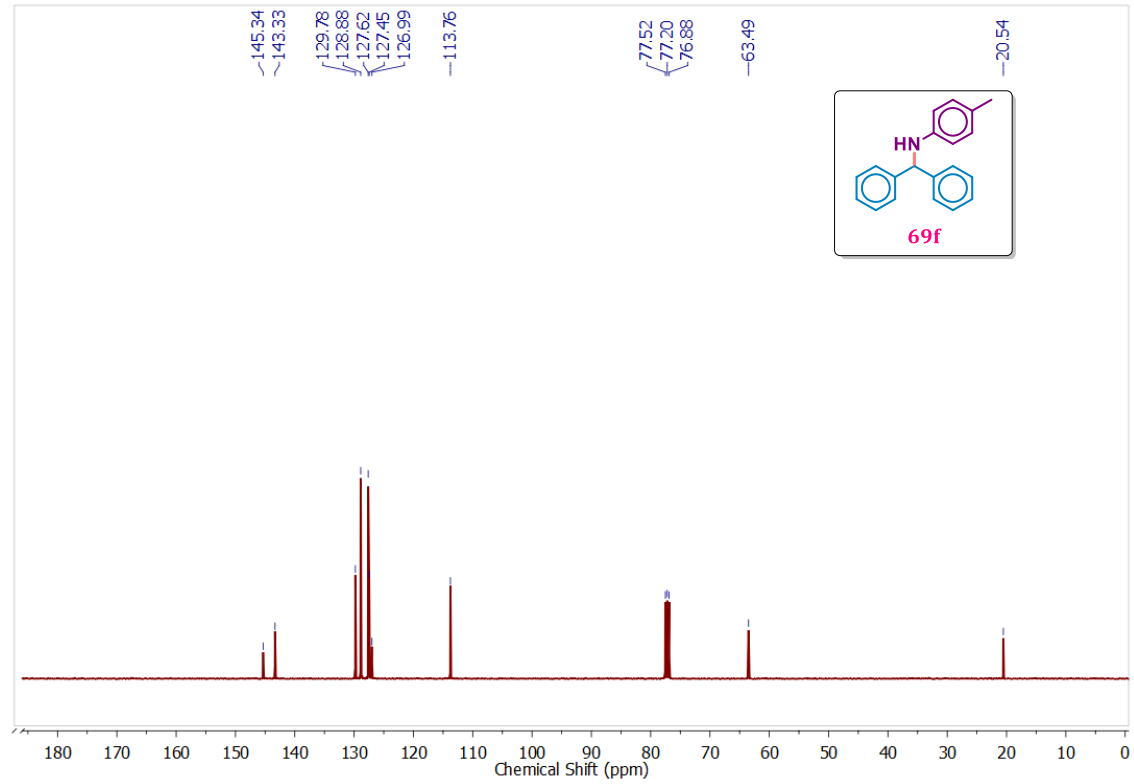

Figure 5.18 $^{13}C\{^{1}H\}$ NMR (101 MHz, $CDCl_3$, 298 K) of **69f**